JOURNAL OF GEOPHYSICAL RESEARCH, VOL. 112, D12S09, doi:10.1029/2006JD007606, 2007

Multi-grid-cell validation of satellite aerosol property retrievals in INTEX/ITCT/ICARTT 2004

P. B. Russell,[1] J. M. Livingston,[2] J. Redemann,[3] B. Schmid,[3] S. A. Ramirez,[3] J. Eilers,[1] R. Kahn,[4] D. A. Chu,[5] L. Remer,[5] P. K. Quinn,[6] M. J. Rood,[7] and W. Wang[7]

Received 31 May 2006; revised 13 October 2006; accepted 5 December 2006; published 8 May 2007.

[1] Aerosol transport off the US Northeast coast during the Summer 2004 International Consortium for Atmospheric Research on Transport and Transformation (ICARTT) Intercontinental Chemical Transport Experiment (INTEX) and Intercontinental Transport and Chemical Transformation (ITCT) experiments produced a wide range of aerosol types and aerosol optical depth (AOD) values, often with strong horizontal AOD gradients. In these conditions we flew the 14-channel NASA Ames Airborne Tracking Sun photometer (AATS) on a Jetstream 31 (J31) aircraft. Legs flown at low altitude (usually $\leq$100 m ASL) provided comparisons of AATS AOD spectra to retrievals for 90 grid cells of the satellite radiometers MODIS-Terra, MODIS-Aqua, and MISR, all over the ocean. Characterization of the retrieval environment was aided by using vertical profiles by the J31 (showing aerosol vertical structure) and, on occasion, shipboard measurements of light scattering and absorption. AATS provides AOD at 13 wavelengths λ from 354 to 2138 nm, spanning the range of aerosol retrieval wavelengths for MODIS over ocean (466–2119 nm) and MISR (446–866 nm). Midvisible AOD on low-altitude J31 legs in satellite grid cells ranged from 0.05 to 0.9, with horizontal gradients often in the range 0.05 to 0.13 per 10 km. When possible, we used ship measurements of humidified aerosol scattering and absorption to estimate AOD below the J31. In these cases, which had J31 altitudes 60–110 m ASL (typical of J31 low-altitude transects), estimated midvisible AOD below the J31 ranged from 0.003 to 0.013, with mean 0.009 and standard deviation 0.003. These values averaged 6% of AOD above the J31. MISR-AATS comparisons on 29 July 2004 in 8 grid cells (each $\sim$17.6 km $\times$ 17.6 km) show that MISR versions 15 and 16 captured the AATS-measured AOD gradient (correlation coefficient R^2 = 0.87 to 0.92), but the MISR gradient was somewhat weaker than the AATS gradient. The large AOD (midvisible values up to $\sim$0.9) and differing gradients in this case produced root-mean-square (RMS) MISR-AATS AOD differences of 0.03 to 0.21 (9 to 31%). MISR V15 Ångstrom exponent α (= $-$dlnAOD/dlnλ) was closer to AATS than was MISR V16. MODIS-AATS AOD comparisons on 8 overpasses using 61 grid cells (each nominally 10 km $\times$ 10 km) had $R^2 \sim 0.97$, with RMS AOD difference $\sim$0.03 ($\sim$20%). About 87% of the MODIS AOD retrievals differed from AATS values by less than the predicted MODIS over-ocean uncertainty, $\Delta\tau = \pm 0.03 \pm 0.05\tau$. In contrast to the small MODIS-AATS differences in AOD, MODIS-AATS differences in Ångstrom exponent α were large: RMS differences for α(553, 855 nm) were 0.28 for MODIS-Terra and 0.64 for MODIS-Aqua; RMS differences for α(855, 2119 nm) were larger still, 0.61 for MODIS-Terra and 1.14 for MODIS-Aqua. The largest MODIS-AATS Ångstrom exponent differences were associated with small AOD values, for which MODIS AOD relative uncertainty is large. Excluding cases with AOD(855 nm) < 0.1 reduced MODIS-AATS α differences substantially. In one grid cell on 21 July 2004, smoke over cloud appeared to impair the MODIS-Aqua cloud mask, resulting in retrieved AODs that significantly exceeded AATS values. Experiments with extending MODIS

[1]NASA Ames Research Center, Moffett Field, California, USA.
[2]SRI International, Menlo Park, California, USA.
[3]Bay Area Environmental Research Institute, Sonoma, California, USA.
[4]Jet Propulsion Laboratory, California Institute of Technology, Pasadena, California, USA.
[5]Laboratory for Atmospheres, NASA Goddard Space Flight Center, Greenbelt, Maryland, USA.
[6]Pacific Marine Environmental Laboratory, NOAA, Seattle, Washington, USA.
[7]Department of Civil and Environmental Engineering, University of Illinois at Urbana-Champaign, Urbana, Illinois, USA.

0148-0227/07/2006JD007606$09.00

retrievals into the glint mask yielded MODIS AODs consistently less than AATS AODs, especially at long wavelength, indicating that the current MODIS glint mask limits should not be reduced to the extent tried here. The sign of the AOD differences within the glint mask (MODIS AOD < AATS AOD) is consistent with ship-measured wind speeds there.

Citation: Russell, P. B., et al. (2007), Multi-grid-cell validation of satellite aerosol property retrievals in INTEX/ITCT/ICARTT 2004, *J. Geophys. Res.*, *112*, D12S09, doi:10.1029/2006JD007606.

1. Introduction

[2] In summer 2004 the International Consortium for Atmospheric Research on Transport and Transformation (ICARTT [*Fehsenfeld et al.*, 2006]) studied air quality, intercontinental transport, and radiative energy budgets in air masses moving across the United States and over the Atlantic Ocean to Europe. Among other experiments, ICARTT included Phase A of the Intercontinental Chemical Transport Experiment (INTEX-A [*Singh et al.*, 2006]) and the Intercontinental Transport and Chemical Transformation (ITCT) experiment. Conditions during ICARTT included transport of a variety of aerosol types off the U.S. northeast coast, which produced a wide range of aerosol optical depth (AOD) values, as well as many cases of horizontal gradients in AOD over the Gulf of Maine. The aerosol types included biomass smoke transported from wildfires in Alaska and western Canada as well as particles in urban and power plant plumes transported from nearby sources on the New England coast and more distant sources in the Ohio River Valley.

[3] In this context, with support from INTEX-A and ITCT, the twin turboprop Jetstream 31 (J31) aircraft flew missions over the Gulf of Maine in July and August 2004. Its goal was to characterize aerosol, water vapor, cloud, and ocean surface radiative properties and effects in flights that sampled polluted and clean air masses in coordination with measurements by other INTEX/ITCT/ICARTT platforms, including aircraft, a ship, and several satellites. Specific science objectives of the J31 included validating satellite retrievals of AOD spectra and of water vapor columns, as well as measuring aerosol effects on radiative energy fluxes. This paper reports J31 AOD measurements and compares them to AOD retrievals by three satellite sensors: the Multiangle Imaging SpectroRadiometer (MISR [*Diner et al.*, 1998; *Martonchik et al.*, 1998]) on the satellite Terra and two Moderate Resolution Imaging Spectroradiometer (MODIS [*Kaufman et al.*, 1997]) instruments, one each on the satellites Terra and Aqua. *Livingston et al.* [2007] report the J31 water vapor measurements and comparisons to satellites and in situ measurements. *Redemann et al.* [2006a] report the J31 measurements of aerosol effects on radiative energy fluxes.

[4] The MISR and MODIS sensors have been producing AOD products for over six years, and these products have been the subject of several validation papers [e.g., *Remer et al.*, 2002, 2005; *Chu et al.*, 2002, 2005; *Levy et al.*, 2003; *Livingston et al.*, 2003; *Schmid et al.*, 2003a; *Martonchik et al.*, 2004; *Abdou et al.*, 2005; *Kahn et al.*, 2005; *Redemann et al.*, 2005, 2006b]. These papers have addressed both AOD and its dependence on wavelength λ, usually expressed as an Ångstrom exponent α (= $-$dlnAOD/dlnλ, in one or more wavelength ranges). Nevertheless, there is a continuing need for ongoing validation studies for several reasons including the following:

[5] 1. The scatterplots that are a staple of the validation studies cited above include points that fall outside the expected ±one-sigma uncertainty. Measurement results that help reveal what causes these outliers can often lead to improved satellite retrievals, which in turn can bring more points within the expected uncertainty.

[6] 2. New versions of satellite AOD products are being developed, and continuing validation measurements are required to inform and to evaluate these new versions, and to test aerosol types and surface conditions not captured in previous campaign events.

[7] 3. Although *Remer and Kaufman* [2006, Figure 10] show good agreement between global, monthly mean level 3 AOD(0.55 μm) from MODIS-Terra and MODIS-Aqua, several other studies have reported persistent differences among the archived products for AOD and Ångstrom exponent from MODIS-Terra, MODIS-Aqua, and MISR. For example, *Redemann et al.* [2004] and *Redemann* [2004] investigated regional maps of monthly mean AOD as provided by the MODIS-Terra and MISR satellite sensors for the month of April during the years 2000–2004. The comparisons showed significant differences in the geographic distribution of the Asian aerosol plume as it advected across the Pacific Ocean in any given year. This was particularly true for April 2001, when the ACE-Asia campaign [*Huebert et al.*, 2003] took place. In 2001, the longitudinally averaged midvisible AOD between 40°N and 50°N as derived by the two sensors differed by more than 20% (or 0.1). Two other studies [*Gassó et al.*, 2004; *Anderson et al.*, 2005] also analyzed the performance of MODIS-Terra during ACE-Asia by comparing the MODIS-derived AOD [*Chu et al.*, 2005], Ångstrom parameter and fine mode fraction to suborbital data. Those studies found generally close agreement between MODIS and the suborbital data for AOD, but much less agreement for the Ångstrom parameter and fine mode fraction. More recently *Redemann et al.* [2006b] found significant differences between MODIS-Terra and MODIS-Aqua level 2 retrievals for both AOD and Ångstrom exponent in terms of their comparison to airborne Sun photometer measurements in April 2004 in the presence of mineral dust. Possible reasons for the above differences include differences in absolute calibration scales and in cloud screening; they are the subject of ongoing studies by the MODIS and MISR teams. Additional validation measurements are important to advancing those studies.

[8] 4. As stressed by *Anderson et al.* [2005], there is a need for increased emphasis on validation of satellite-retrieved Ångstrom exponent, which is closely related to

aerosol fine mode fraction and submicron fraction, and hence to designation of aerosols as anthropogenic versus natural. Studies that have compared satellite and suborbital results for Ångstrom exponent [e.g., *Levy et al.*, 2003; *Livingston et al.*, 2003] have found significant differences in some situations. *Gassó and O'Neill* [2006] emphasized that aerosol fine mode fraction retrieved from AOD spectra describing a column cannot be used to distinguish whether the aerosol under observation is composed of layers each with distinctive modal features or all layers with the same modal features.

[9] 5. The workhorse of most satellite AOD validation studies, Sun photometry at fixed ground sites, is not well suited to acquiring data over the open ocean or to examining the ability of satellite retrievals to provide consistent results across grid cell boundaries, to measure horizontal gradients accurately, and to perform well when aerosols occur in several overlapping atmospheric layers with different properties in different layers. Airborne Sun photometry is uniquely able to address these gaps and also to measure AOD variability within satellite grid cells, to check for systematic AOD increases when approaching clouds, and to determine the spatial scale of such increases if they exist. Its use in well designed field studies can refine and validate the satellite retrieval algorithms and also help develop ways to combine the less detailed but more extensive satellite observations with detailed constraints on AOD, Ångstrom exponent, absorption, composition and their vertical and horizontal variability using the aircraft-acquired information.

2. Data Sources and Analysis Methods

2.1. Airborne Sun Photometer

[10] The NASA Ames Airborne Tracking Sun photometer (AATS-14), which flew on the J31, measures transmission of the direct solar beam in 14 channels with center wavelengths ranging from 354 to 2138 nm. This wavelength range includes the aerosol retrieval wavelength range for MODIS over ocean (466–2119 nm) and for MISR (446–866 nm). The AATS-14 instrument, data recording, and cloud screening procedures are described by *Schmid et al.* [2000, 2003a, 2003b] and *Russell et al.* [2005]. Our methods for further data reduction, calibration, and error analysis are described by *Russell et al.* [1993a, 1993b], *Schmid and Wehrli* [1995], and *Schmid et al.* [1996, 1998, 2001, 2003a, 2003b]. The AATS-14 channels are chosen to permit separation of aerosol, water vapor, and ozone attenuation along the measured slant path. From these slant-path transmissions we retrieve AOD (also denoted $\tau_p(\lambda)$) in 13 narrow wavelength bands (centered at 354, 380, 453, 499, 519, 604, 675, 778, 865, 1019, 1241, 1558, and 2139 nm, with full-width-half-maximum bandwidths of 2.0, 4.6, 5.6 5.4, 5.4, 4.9, 5.2, 4.5, 5.0, 5.1, 5.1 4.9, and 17.3 nm, respectively) and the columnar amounts of water vapor (from the channel centered at 941 nm). For suitable conditions (basically solar zenith angle $>\sim 80^\circ$ and AOD(600 nm) $<\sim 0.04$) we can also retrieve ozone column content. For other conditions (including those in ICARTT), we use ozone column amounts from TOMS satellite retrievals. Resulting ozone-induced uncertainties in AOD are included in our error bars and are always <0.01 at 600 nm and less at other wavelengths.

[11] In addition to the corrections for Rayleigh scattering and O_3 absorption, measurements in some AATS-14 channels require corrections for NO_2, H_2O and O_2-O_2 absorption in order to retrieve AOD. These corrections were performed as described by *Schmid et al.* [2006].

[12] AATS was calibrated by analysis of sunrise measurements acquired at Mauna Loa Observatory (MLO), Hawaii, before the INTEX/ITCT/ICARTT deployment and also by analysis of sunset measurements acquired on 4 special J31 flights during INTEX/ITCT/ICARTT. Exoatmospheric detector voltages, V_0, were derived using the Langley plot technique [e.g., *Russell et al.*, 1993a, 1993b; *Schmid and Wehrli*, 1995] for all channels except 941 nm, for which a modified Langley technique was employed to account for water vapor absorption [*Reagan et al.*, 1995; *Michalsky et al.*, 1995; *Schmid et al.*, 1996, 2001]. Resulting uncertainties in AOD are typically less than 0.01, and are shown by error bars on selected plots in this paper.

[13] A potentially large source of calibration error is dirt deposited on the Sun photometer entrance window [e.g., *Livingston et al.*, 2003]. To minimize this error we cleaned the window carefully before each flight and inspected it carefully for dirt after each flight.

[14] We derived profiles of aerosol extinction $\sigma_{ep}(\lambda)$ for many profiles by vertically differentiating the $\tau_p(\lambda)$ profiles (after discarding profiles influenced by considerable horizontal inhomogeneity or overlying clouds). An example is shown in section 3.3.

[15] Because most of the errors in $\tau_p(\lambda)$ are of systematic nature, they cancel when differences (such as layer $\tau_p(\lambda)$) or differentiations ($\sigma_{ep}(\lambda)$) are used. However, since the aircraft requires a finite time to fly a vertical profile which has a finite horizontal component, temporal and spatial variation of the aerosol above the aircraft will lead to uncertainties in the differentiated quantities.

2.2. Estimating AOD Below the J31 Using Ship Humidified Scattering and Absorption Measurements

[16] Because the J31 flew at a nonzero altitude (typically 60 to 100 m ASL) for the satellite validation measurements reported here, it is desirable to estimate the AOD below the J31. For this purpose we have used aerosol extinction values derived from measurements of aerosol scattering, absorption, scattering humidification, and relative humidity made on the NOAA RV *Ronald H. Brown* (using an inlet at 18 m ASL) during times when the J31 flew by the ship and AATS could view the Sun.

[17] Aerosol scattering coefficients σ_{sp} were measured with an integrating nephelometer at wavelengths 450, 550, and 700 nm, all at instrument relative humidity (RH) ~60%. The nephelometer had a 1.0 μm cutoff diameter at 60% RH. Measured scattering coefficients were corrected for truncation errors and non-Lambertian illumination using the method of *Anderson and Ogren* [1998]. Absorption coefficients $\sigma_{ap}(60\%)$ were measured with a filter-based particle soot absorption photometer at 467, 530, and 600 nm. Calculated Angstrom exponents were used to adjust the absorption coefficients to the nephelometer wavelengths. Scattering, absorption, and ambient RH were measured with a 1 min time resolution. At a slower resolution of ~1 hour, measurements of $f(\mathrm{RH}, \mathrm{RH}_{\mathrm{ref}})$, i.e., the dependence of aerosol scattering σ_{sp} on RH were made using one dry

and one RH-scanning nephelometer [*Carrico et al.*, 2003; *Rood et al.*, 2006] with an inlet cutoff to admit particles with diameters <1 μm at 60% RH.

[18] We estimated ambient scattering, $\sigma_{sp}(RH_{amb})$, from the $\sigma_{sp}(60\%)$ measurements using curves fitted to the $f(RH, RH_{ref})$ data of *Rood et al.* [2006]. We then estimated ambient extinction as

$$\sigma_{ep}(RH_{amb}) = \sigma_{sp}(RH_{amb}) + \sigma_{ap}(60\%), \quad (1)$$

using the common assumption that absorption σ_{ap} is only weakly dependent on RH and can be approximated by its value at 60% RH [e.g., *Redemann et al.*, 2001].

[19] We then estimated AOD below the J31 as

$$AOD_{belowJ31} = \sigma_{ep}(RH_{amb}) z_{J31}, \quad (2)$$

where z_{J31} is the J31 altitude (typically 60 to 100 m ASL in the low-altitude passes of the *Ronald H. Brown* and in the transects used for satellite validation). This approach neglects any RH_{amb} and aerosol variations with altitude below z_{J31}. Results are shown in section 3.1, where we also note that on the three occasions where radiosonde vertical profiles of RH_{amb} were available, using altitude-dependent RH_{amb} in place of the values at the ship's aerosol inlet changed values of $AOD_{belowJ31}$ by less than 15%, with no systematic bias.

[20] Because fog was frequently present at the *Ronald H. Brown* in the 2004 ICARTT measurements, it is important to assess whether fog was present during the periods when we used ship in situ measurements to estimate ambient extinction and AOD below the J31. For three reasons we believe fog was not present during those periods. First, the J31 avoided flying near the *Ronald H. Brown* when *Ronald H. Brown* was in fog, for safety reasons. Second, the ship-measured RH_{amb} values during the six periods were 78%, 88%, 91%, 83%, 81%, and 84%, all well below 100%. Third, ship-derived values of liquid water content were zero, and corresponding values of saturation ratio were less than one, during those periods.

2.3. MISR and MODIS

[21] Aerosol measurements from space are essential to understanding aerosol global and regional distributions, temporal variations, transport, and effects on radiation budgets and climate [e.g., *Ramanathan et al.*, 2001; *Kaufman et al.*, 2002]. MISR and MODIS are part of a new generation of spaceborne sensors with capabilities designed specifically to measure aerosols from space, in contrast to their predecessors AVHRR and TOMS (which have provided many useful, though limited, aerosol measurements in spite of not being designed for this purpose). MISR and MODIS were launched on the EOS Terra satellite in 1999, starting a new era of satellite-based observations of aerosols. A second MODIS was launched on the EOS Aqua satellite in 2002. Terra and Aqua are Sun-synchronous satellites, with Terra's sunlit overpasses occurring in the local morning and Aqua's in the local afternoon. Equator crossing times for Terra and Aqua are ~1030 and ~1330 local time, respectively. Advantages of MODIS [*Kaufman et al.*, 1997] over its predecessors AVHRR and TOMS include its improved spectral coverage, narrower bandwidth of individual channels and improved horizontal resolution of 500 m (250 m for some channels), as compared to 1 km or 4 km for AVHRR and 50 km for TOMS. For MISR [*Diner et al.*, 1998; *Martonchik et al.*, 1998], the improved capabilities further stem from its multiangle viewing technique, which makes it possible to distinguish atmospheric from surface properties and to derive information on particle shape. In general, the improved spatial resolution of the new sensors allows for a better detection of clouds and hence an improved separation of aerosols from clouds. However, the multiangle geometry of MISR affects spatial resolution and increases the complexity of cloud clearing. For example, the MISR standard cloud-clearing includes not only nadir-camera tests, but also angle-by-angle [*Zhao and Di Girolamo*, 2004], angular smoothness [*Martonchik et al.*, 1998], stereo height [*Moroney et al.*, 2002], and band-differenced angular signature [*Di Girolamo and Wilson*, 2003] cloud masks.

[22] The AOD measurements by AATS on the J31 are well suited to studies of satellite retrieval spatial resolution, since they can acquire AOD measurements at a resolution of a few hundred meters and across many satellite retrieval grid cells in a relatively short time (see examples in section 3), something not possible in the usual validation studies that use the fixed, ground-based Sun/sky photometers in the AERONET network.

[23] In this paper, we describe the AATS-14 measurements of AOD during the 2004 INTEX/ITCT/ICARTT experiment, with a special emphasis on assessing the spatial variability of AOD across multiple satellite retrieval grid cells. We include validation measurements for the MODIS and MISR over-ocean AOD retrieval products. There were four AATS-MISR coincidences, on 20, 22 and 29 July and on 7 August 2004. In this paper we focus on the 29 July coincidence. There were eight AATS-MODIS coincidences, on 12, 16, 17, 21, 22 and 23 July and on 2 and 8 August 2004. We describe all 8 of those coincidences in this paper.

2.3.1. MODIS Retrievals of AOD Over the Ocean

[24] In the first step of the MODIS over-ocean algorithm for the retrieval of AOD, the reflectances from the six channels at 553, 644, 855, 1243, 1632 and 2119 nm are grouped into nominal 10 km cells of 20 by 20 pixels at 500 m resolution (with the cross-track dimension stretched as distance from the subsatellite track increases). Cloud masking in the over-ocean AOD algorithm is based on a series of tests that use reflectances at 466, 553, 644, 1243, and 1380 nm. An important test uses the standard deviation of 553 nm reflectances in every group of 3 by 3 pixels within a cell [*Remer et al.*, 2005; *Martins et al.*, 2002]. If any such group has standard deviation greater than 0.0025, the center pixel in the group is initially labeled as cloud. Further tests using other wavelengths are employed to help prevent inhomogeneous aerosol fields (e.g., dust) from being identified as clouds, and to help prevent spatially homogeneous clouds (e.g., cirrus and the centers of large, thick clouds) from being identified as aerosol [e.g., *Gao et al.*, 2002; *Remer et al.*, 2005].

[25] After the application of the various cloud masks, a sediment mask is applied, after which the brightest 25% and darkest 25% (at 855 nm) of the remaining pixels are discarded. The reflectances in the remaining pixels are averaged and compared to a look-up table, consisting of

four fine and five coarse mode aerosol types [*Remer et al.*, 2005]. All combinations of fine and coarse modes that fit the measured reflectances to within 3% (or the best three combinations if no solution matches the reflectances to within 3%) are then averaged to yield the average combination of fine and coarse mode aerosol. Over ocean, AOD products are produced at the six measurement wavelengths, 553, 644, 855, 1243, 1632 and 2119 nm, and also at 466 nm by using the model(s) that best fit the measured reflectances.

[26] Initial validation efforts of the MODIS level 2 aerosol data product were carried out by *Remer et al.* [2002, 2005], *Levy et al.* [2003], *Livingston et al.* [2003], and *Levy et al.* [2005]. *Remer et al.* [2005] found that one standard deviation of all MODIS-Terra AOD retrievals (when compared to AERONET AOD measurements) fall within the predicted uncertainty $\Delta\tau = \pm 0.03 \pm 0.05\tau$ over ocean and $\Delta\tau = \pm 0.05 \pm 0.15\tau$ over land. Recently, *Ichoku et al.* [2005] validated both MODIS-Terra and MODIS-Aqua aerosol data. They found no significant difference in the performance of MODIS-Terra and MODIS-Aqua for determining AOD between 466 and 855 nm. All these validation studies used the validation approach developed by *Ichoku et al.* [2002], which averages MODIS data over nominally 50 × 50 km boxes and AERONET measurements over 1 h. More recently *Redemann et al.* [2006b], working at the nominal level 2 retrieval scale of 10 km × 10 km, found significant differences between MODIS-Terra and MODIS-Aqua retrievals for both AOD and Ångstrom exponent in terms of their comparison to airborne Sun photometer measurements made in April 2004 in the presence of mineral dust. Other studies [e.g., *Levy et al.*, 2003; *Livingston et al.*, 2003] also found MODIS retrievals of Ångstrom exponent that differed significantly from suborbital results, possibly as a result of dust nonsphericity.

[27] The Scientific Data Sets (SDS) within the MODIS level 2 aerosol data products (MOD04_L2 for Terra and MYD04_L2 for Aqua) we specifically consider in this paper are the AOD at 466, 553, 644, 855, 1243, 1632 and 2119 nm [Effective_Optical_Depth_Average_Ocean], the Ångstrom exponent between 553 and 855 nm [Ångstrom_Exponent_1_Ocean(2)], and the Ångstrom exponent between 855 and 2119 nm [Ångstrom_Exponent_2_Ocean(2). The index (2) in the Ångstrom exponents denotes that this variable is the average of a number of solutions that best matched the measured radiances, instead of being the single best solution.

2.3.2. MISR Retrievals of AOD

[28] MISR produces 36 simultaneous views of Earth, in a combination of nine angles varying from +70° to −70° in the along-track direction, in four spectral bands centered at 0.446, 0.558, 0.672 and 0.867 μm [*Diner et al.*, 1998]. It takes 7 min for all nine MISR cameras to view a fixed line on the surface, which sets the effective temporal resolution for coincident observations. At midlatitudes, a given location is imaged about once per week in Global Mode, providing 275 m resolution data in all four nadir channels, and in the red channels of the other eight cameras. The remaining 24 channels of data are averaged on board the spacecraft to 1.1 km resolution. For three MISR event days during ICARTT (20, 22, and 29 July), the Gulf of Maine was also designated as a MISR Local Mode site, 300 km along-track by 360 km cross-track, over which data were acquired at 275 m resolution in all 36 channels.

[29] Prelaunch theoretical studies indicated that MISR spectral radiances, measured at precisely known air mass factors ranging from one to three, could provide tight constraints on AOD over land and water [*Martonchik et al.*, 1998]. Because of the wide range of scattering angles sampled (about 50° to 160° at midlatitudes), MISR also offers constraints on particle shape, size distribution, and single scattering albedo, particularly over dark, uniform ocean surfaces [*Kahn et al.*, 2001a; *Kalashnikova and Kahn*, 2006].

[30] This study is one of many that involve actual field campaign data to assess the sensitivity of aerosol retrievals on the basis of satellite multiangle imaging. In addition, the assumptions made in the retrieval algorithm about aerosol component particle properties, scene variability, and other factors, must be critically tested and refined. Together with studies from SAFARI, ACE-Asia, and CLAMS [e.g., *Schmid et al.*, 2003a, 2003b; *Kahn et al.*, 2004; *Redemann et al.*, 2003, 2005; *Smith et al.*, 2005], the current study is part of an ongoing MISR validation effort that is aimed in part at defining a few satellite scenes very carefully and in detail to then use the findings regarding performance to refine the aerosol retrieval algorithm applied globally. The validation program also compares, statistically, MISR retrieval results with other large aerosol data sets [e.g., *Abdou et al.*, 2005; *Kahn et al.*, 2005]. Since scene variability was determined in prelaunch studies to contribute significantly to the uncertainties in the aerosol retrievals [*Kahn et al.*, 2001b] and since AOD variability is one of the main contributors to scene variability over the ocean, the analysis of spatial variability of AOD over multiple MISR retrieval grid cells performed in this paper supports the assessment of MISR aerosol retrieval algorithm performance.

3. Results

3.1. Comparison of AOD Above and Below the J31 Using AATS and Ship Humidified Scattering and Absorption

[31] Figure 1 shows results for AOD(500 nm) above and below the J31 for six cases where the J31 flew by the ship at low altitude (60 to 110 m ASL). AOD above the J31 was calculated from AATS measurements as described in section 2.1. AOD below the J31 was calculated from ship humidified scattering and absorption measurements as described in section 2.2, and interpolated to wavelength 500 nm. Note that in all six cases AOD(500 nm) below the J31 is very small compared to AOD(500 nm) above the J31. AOD(500 nm) below the J31 ranged from 0.003 to 0.013, with mean value 0.009 and standard deviation 0.003. These values are comparable to the typical Sun photometer calibration uncertainty of ∼0.01. The ratios of AOD(500 nm) below the J31 to AOD(500 nm) above the J31 ranged from 1.0% to 13.9%, with mean value 6.2% and standard deviation 4.8%.

[32] Figure 2 shows AOD spectra above and below the J31 for the six cases in Figure 1. In terms of the ratio of AOD below the J31to AOD above it, results at 450, 550, and 700 nm are similar to those quoted in connection with Figure 1 for 500 nm. For all six cases Table 1 shows the

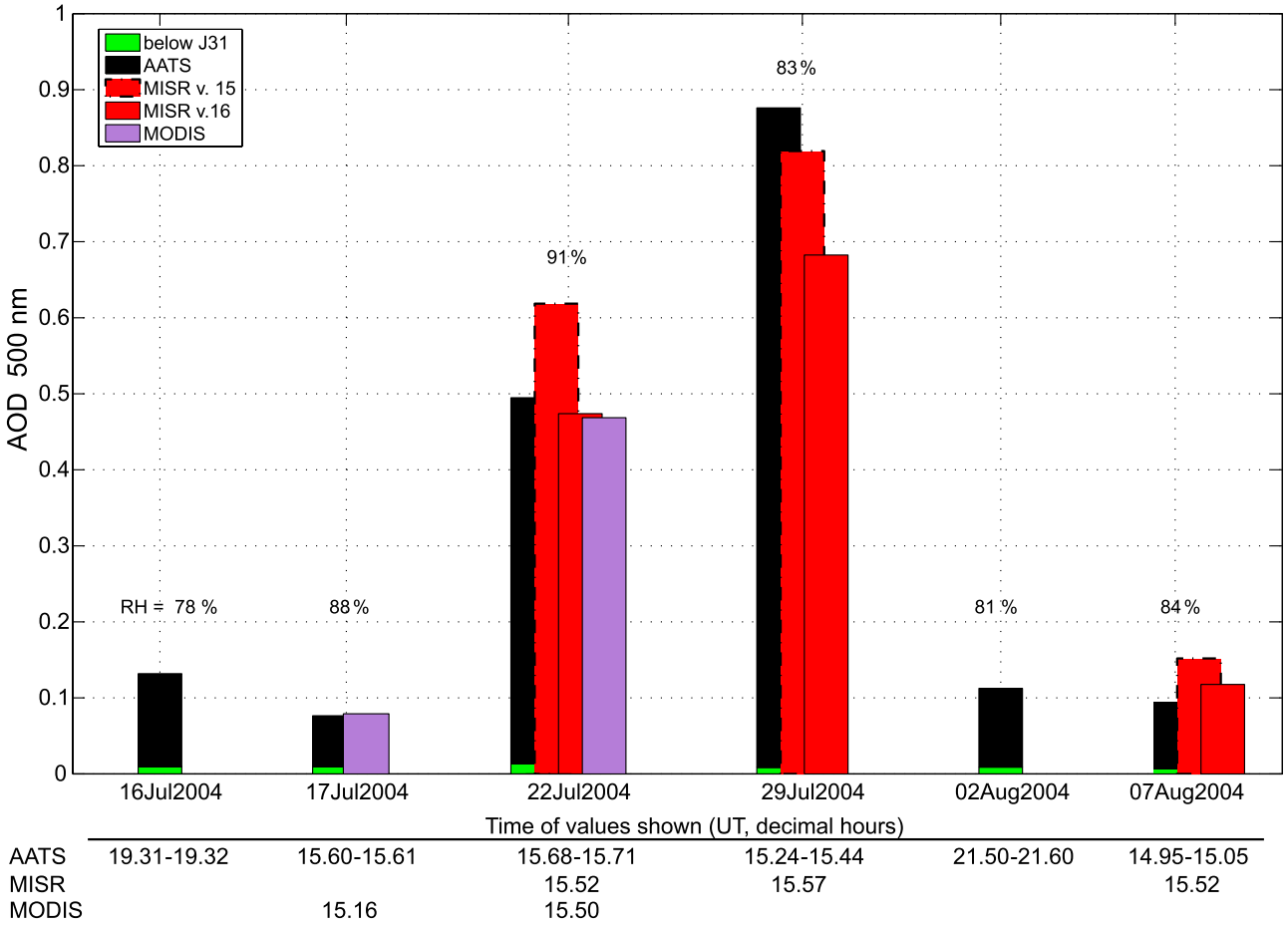

Figure 1. Comparison of AOD(500 nm) below J31 (estimated from measurements of humidified scattering and absorption made on the ship *Ronald H. Brown*), above J31 (from AATS measurements), and below satellites (from MODIS and MISR retrievals). Numbers below date labels give time (in decimal hours UT) of each measurement.

range, mean, and standard deviation of the ratio of AOD below to above the J31 for all four wavelengths 450, 500, 550, and 700 nm. Including all wavelengths, the mean ratio of AOD below to above the J31 ranged from 5.9% to 6.3% with standard deviation 4.5% to 5.4%.

[33] As noted in section 2.2, our procedure to obtain the above results for AOD below the J31 neglects any RH_{amb} and aerosol variations with altitude below z_{J31}. On three of the cases shown in Figures 1 and 2 (16 and 29 July and 7 August), radiosonde vertical profiles of RH_{amb} were available near the time of the J31 flyby. For those cases, we used altitude-dependent RH_{amb} in place of the values at the ship's aerosol inlet (which was at 18 m ASL). Results for $AOD_{belowJ31}$ differed from the values in Figures 1 and 2 by less than 15%, with no systematic bias (i.e., the results with altitude-dependent RH_{amb} were smaller on 16 July and 7 August and larger on 29 July).

[34] In connection with the above comparisons between AATS and ship AOD values it is relevant to mention the considerable history of previous comparisons between airborne AATS AOD measurements and surface-based Sun photometer or radiometer measurements of AOD in several field campaigns (e.g., *Schmid et al.* [2000] in ACE-2, *Schmid et al.* [2003a, 2003b] in SAFARI-2000, *Livingston et al.* [2003] in PRIDE, *Redemann et al.* [2005] in CLAMS, and *Schmid et al.* [2006] in DOE-ARM AIOP), which showed very good agreement (i.e., RMS differences $\leq$0.01). In the current study we have not used ship-estimated AOD below the J31 to increase AATS-measured AODs, because the ship-estimated AODs are small (mean 0.009 at 500 nm), varied significantly (from 0.003 to 0.013 at 500 nm), covered only a small subset of AATS wavelengths (450–700 nm out of 354–2119 nm), and were not available for many AATS low-altitude transects.

3.2. MISR-AATS Comparisons

[35] Figure 3 shows a MISR image from the overpass on 29 July 2004 at 1534 UT (15.57 UT in decimal hours), along with the J31 flight track. (In this paper, all times with decimal points are in decimal hours, and times without decimal points are HHMM, where HH is hours and MM is minutes. We use both because decimal hours provide the most convenient time axis in plots, whereas satellite and other data are often archived in HHMM format. All times in this paper are in Universal Time (UT).) The MISR image, from camera Aa (i.e., looking forward along the satellite track at 26° from nadir) shows the Gulf of Maine off the New Hampshire and Maine coasts, as well as the clouds that

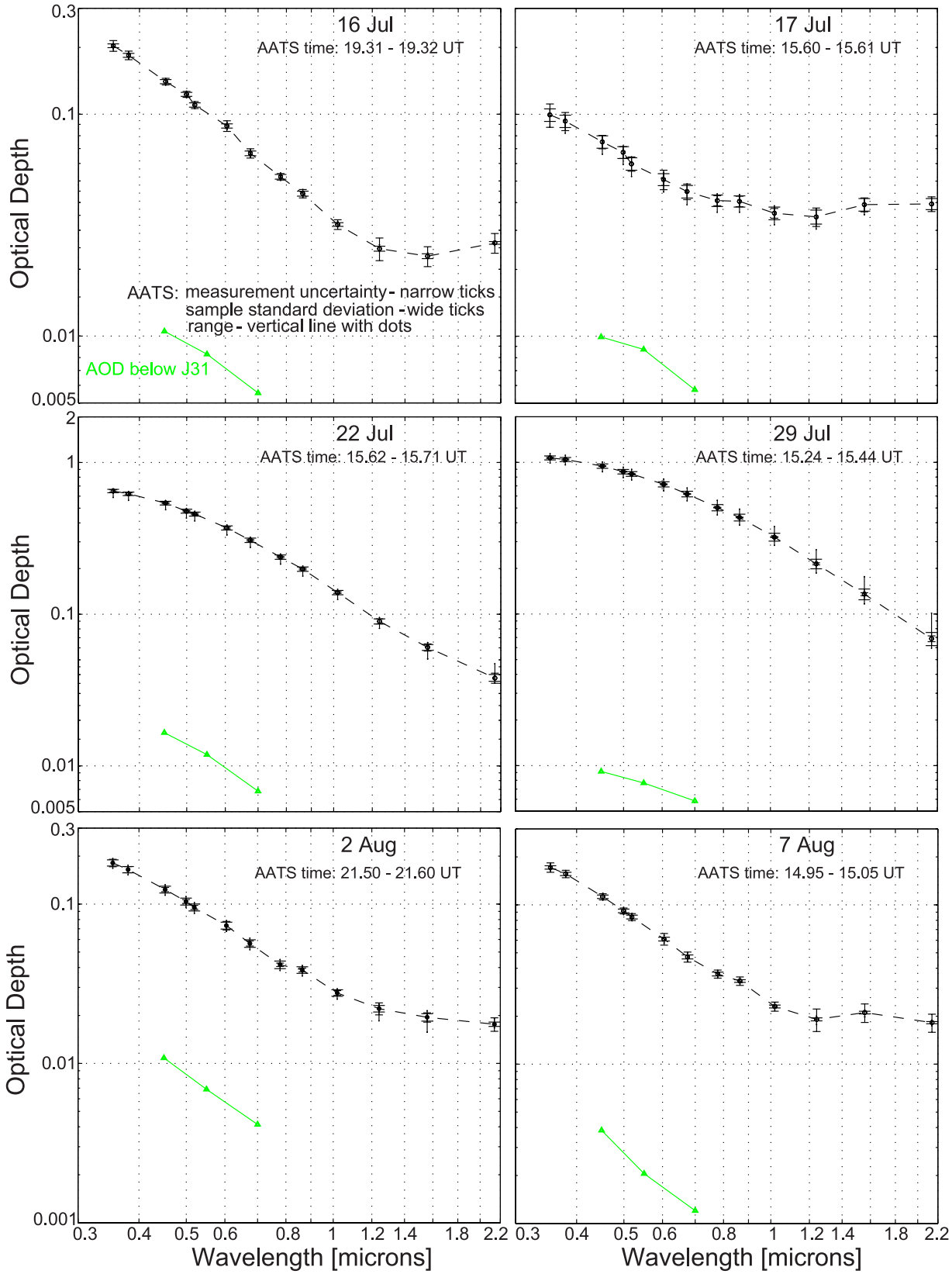

Figure 2. AOD spectra for the cases in Figure 1. AATS AODs shown are as measured, i.e., describing the column above the J31, with no estimate of AOD below the J31 added. Note different AOD scales in middle row to accommodate large AODs on 22 and 29 July.

Table 1. Ratio of AOD Below to Above the J31

	Wavelength, nm			
	450	500	550	700
Range, %	1.0–13.1	1.0–13.9	1.0–15.4	1.0–13.1
Mean, %	6.1	6.2	6.3	5.9
st_dev, %	4.5	4.8	5.4	4.7

were prevalent on this day (and on many other days during ICARTT).

[36] Figure 4 (top) shows a more detailed view of the minimum-altitude J31 legs. In this view, any point along the J31 path is omitted if clouds are impacting AATS's view of the Sun, and also if the J31 altitude exceeds 100 m (which typically occurred during J31 turns). It can be seen that the AATS viewing path was cloud-impacted at Terra overpass time (15.57 UT), but largely cloud-free on the legs before and after that time. All AATS measurements considered in this section were taken within 30 min of satellite overpass time.

[37] Also shown in Figure 4 (top) are the grid cells in which MISR Standard Algorithm AOD retrievals were possible. The J31 flew through 8 such MISR grid cells at altitudes $\leq$100 m and within 30 min of satellite overpass time. Figure 4 (bottom) shows AATS-measured multiwavelength AODs along the J31 track flown from ~15.25 to 16.0 UT. These results show a strong gradient in AOD, with AOD(499 nm) decreasing from ~0.8 to ~0.38 when flying west along the northernmost leg (15.6 to ~15.77 UT), and then increasing from ~0.38 to ~1.1 when flying east-southeast along the southern leg (15.79–16.0 UT). Colored vertical lines in Figure 4 (bottom) show the times when the J31 crossed the edge of a MISR grid cell. The colors of the vertical lines in Figure 4 (bottom) match those of the grid cells in Figure 4 (top). (Absence of a grid cell along a J31 flight segment indicates absence of a MISR Standard Aerosol retrieval there. Currently, the Standard algorithm requires that at least 32 of 256 1.1 km pixels in each 17.6 × 17.6 km cell must pass tests for cloud masking, spatial correlation, and angular smoothness.)

[38] Figure 5 compares AATS and MISR V15 AOD spectra. A MISR spectrum is shown for each of the 8 colored grid cells in Figure 4. AATS spectra are shown in Figure 5 only as the mean from the whole flight path of Figure 4, along with the typical AATS measurement uncertainty (narrow ticks), standard deviation of results along the flight path (wide ticks), and range along the flight path (vertical bars). The inset time series in Figure 5 shows that MISR V15 spectra have the same sign of gradient as AATS. For example, the inset time series shows AATS AOD decreasing in going from red cell to yellow cell to green cell to blue cell. The MISR spectra in the main figure show the same thing: decreasing AOD in going from red spectrum to yellow spectrum to green spectrum to blue spectrum.

[39] Figure 6 shows the analogous comparison for MISR V16. V16 retrieved AOD in only 7 cells; however, they show a gradient with the same sign as AATS AOD, analogous to that described above. The V16 MISR Standard Aerosol Retrieval algorithm contains improved medium-

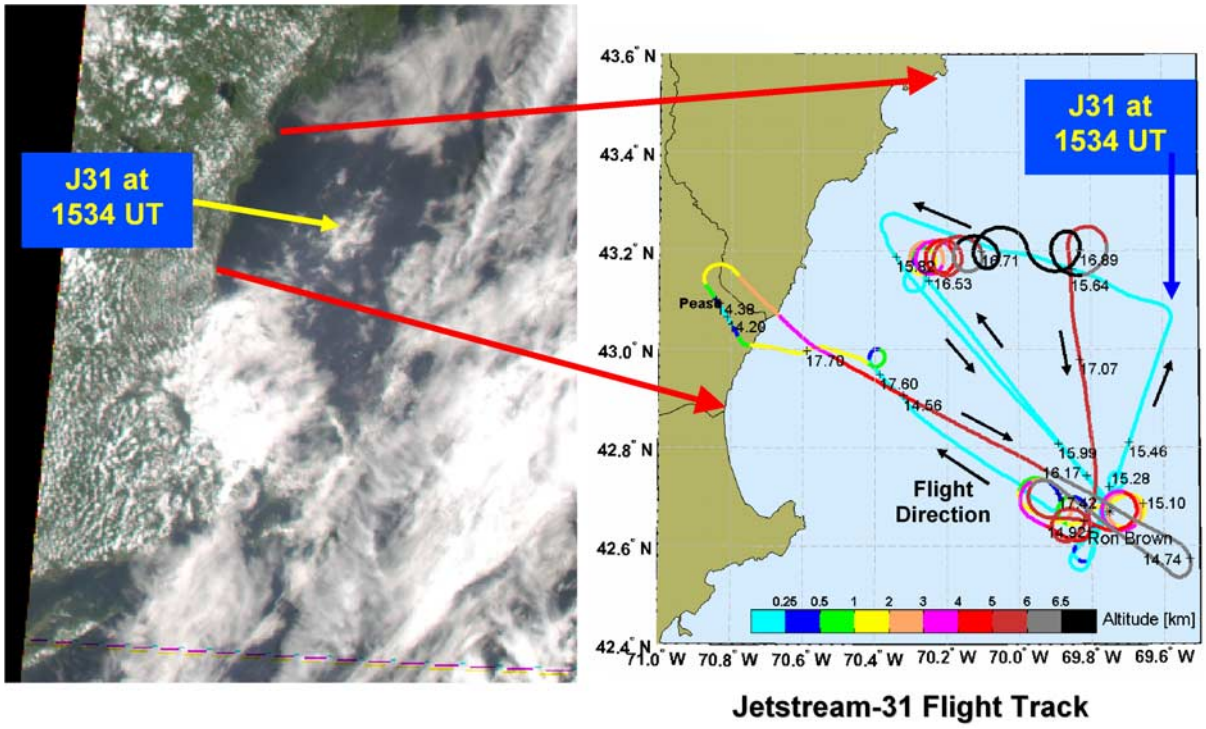

Figure 3. (left) MISR image from camera Aa, level 1B2 RGB, 1534 UT (15.57 UT in decimal hours) on 29 July 2004. Orbit 24542, 1.1 km resolution. (right) J31 flight track, with location at satellite overpass time marked.

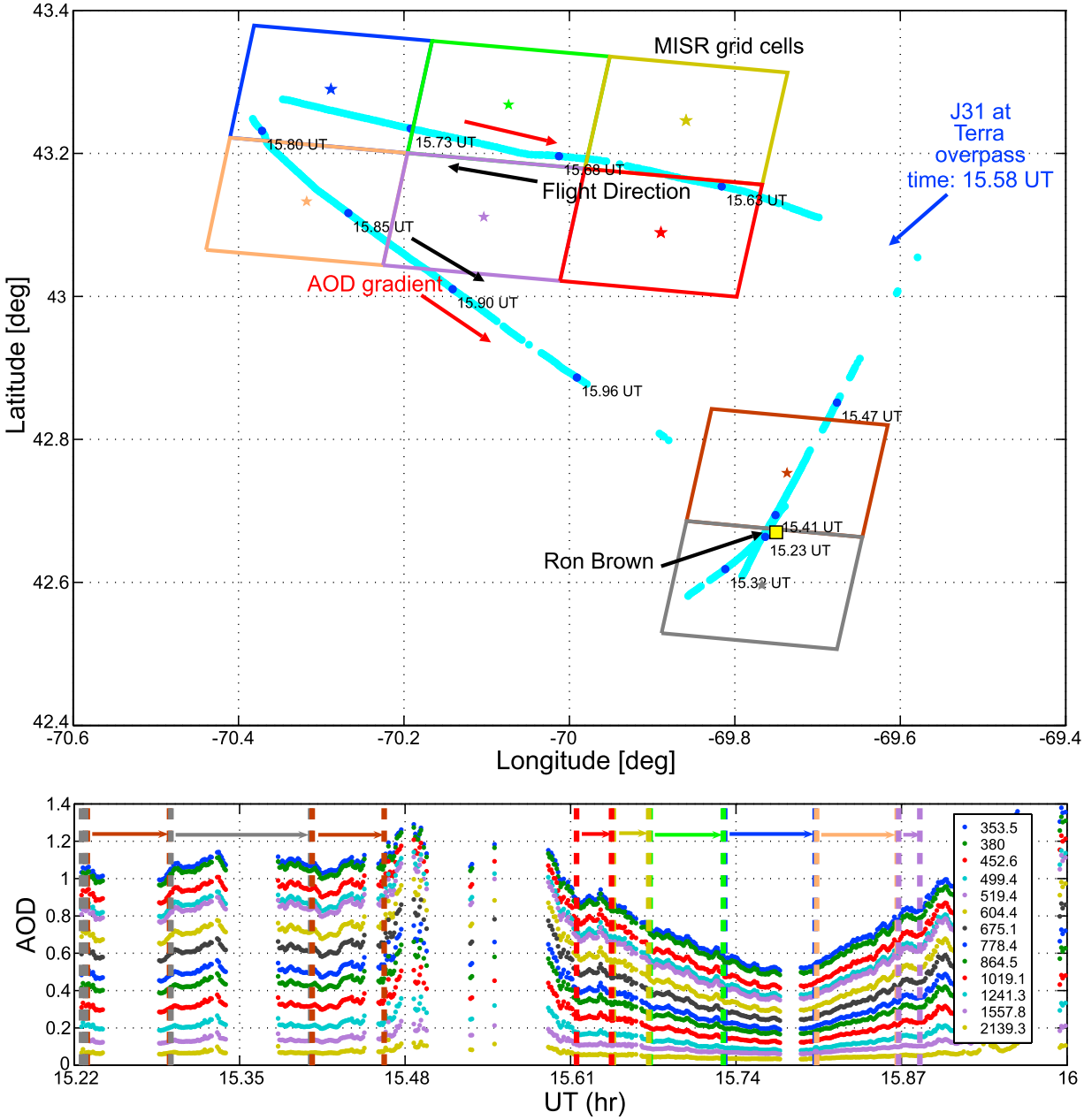

Figure 4. (top) J31 flight path at minimum altitude with superimposed MISR grid cells. Gaps indicate clouds are impacting AATS's view of the Sun, or the J31 altitude exceeds 100 m (which typically occurred during J31 turns). (bottom) AATS-measured multiwavelength AOD along the flight path, showing edges of MISR grid cells and flight direction.

mode dust optical models [*Kalashnikova et al.*, 2005], and additional medium-mode spherical particles having single-scattering albedo 0.80 and 0.90, that replace the tiny black carbon particles in earlier algorithm versions.

[40] Figure 7 uses scatterplots (one for each MISR wavelength) to make a more quantitative comparison of MISR V15 and AATS AODs and their gradients. AATS AODs for each grid cell were obtained by averaging all AATS measurements within the cell to yield a spectrum of ln AOD versus ln λ, which was then fitted with a quadratic least squares fit. From the AATS-derived fit, the AOD at the intermediate MISR wavelengths of 446, 558, 672 and 867 nm was determined. Although several MISR wavelengths are close to AATS-14 wavelengths (see Figures 5 and 6), the fit procedure above was used to minimize the impact of possible AATS-14 single-channel contamination and other uncertainties. and uncertainties stemming from gaseous absorption in the AATS channels, the latter being particularly important at the near-IR wavelengths.

[41] The positive slopes and large R^2 values in Figure 7, 0.91 to 0.92, confirm that MISR V15 is obtaining the same sign of AOD gradient as AATS. However, the fact that the

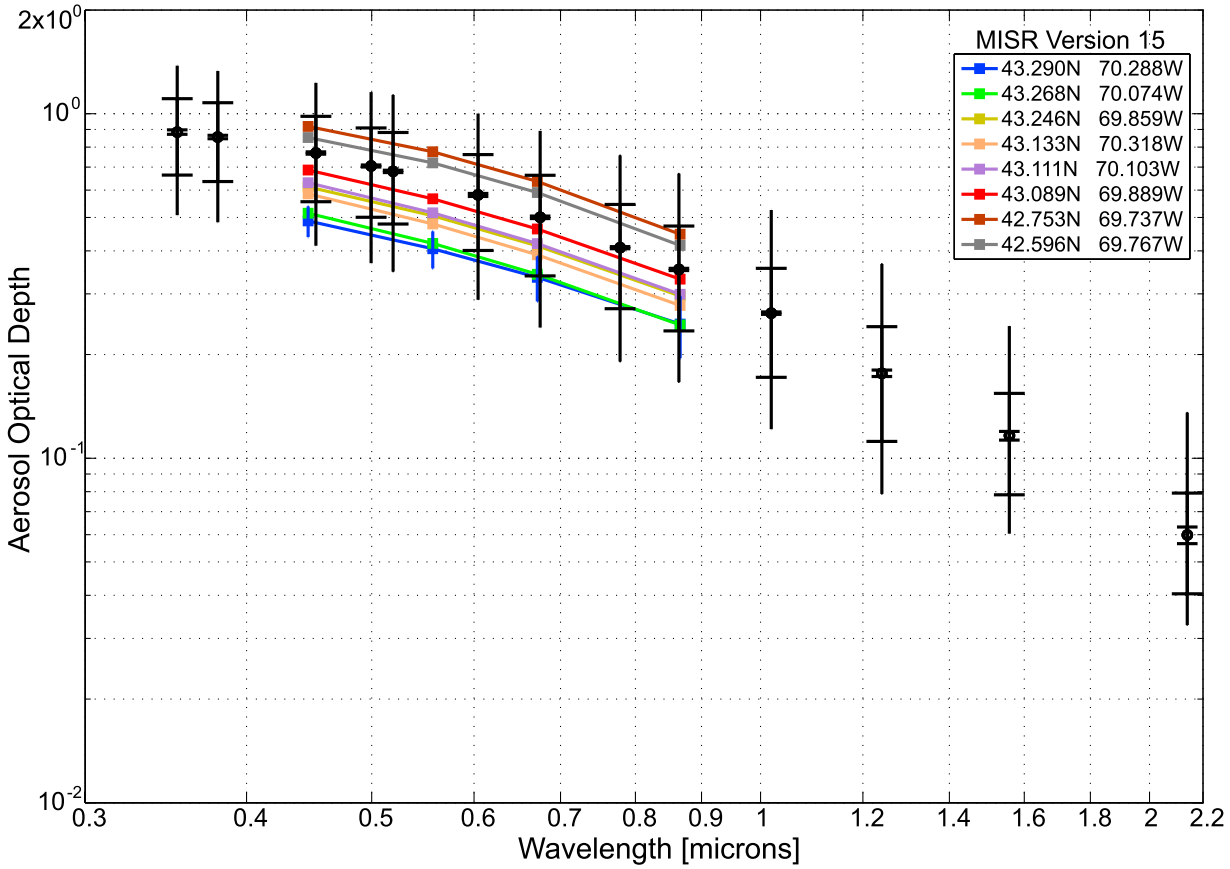

Figure 5. Comparison of AOD spectra measured by AATS and MISR (version 15), 29 July 2004. Colors of MISR spectra match the MISR grid cell colors in Figure 4. The AATS spectrum (open black circles) is a mean from the whole flight path of Figure 4, along with the typical AATS measurement uncertainty (narrow ticks), standard deviation of results along the flight path (wide ticks), and range along the flight path (vertical bars).

slopes are <1 (0.77 to 0.80) shows that the MISR gradient is somewhat weaker than the AATS gradient. The relatively large AOD values (AATS AOD(446 nm) $\sim$ 0.4 to 1.0) and different gradients produce RMS MISR-AATS differences of 0.03 to 0.07 (9 to 11%).

[42] Figure 8 shows analogous scatterplots for MISR V16. In this case slopes range from 0.72 to 0.88, and RMS MISR-AATS differences are 0.03 to 0.21 (11 to 31%).

[43] Taken together, Figures 5–8 show that for the 29 July 2004 MISR-AATS comparison, MISR V15 is closer to AATS than is V16, in terms of both Ångstrom exponent (slope in Figures 5 and 6) and in AOD for most wavelengths (RMS differences in Figures 7 and 8). The larger Ångstrom exponent of MISR V15 AOD results from the V15 retrieved aerosol mixture having smaller particles than V16. The V15 Standard Retrieval mixtures are primarily nonabsorbing spheres with r_{eff} 0.26 μm, with small fractions of spheres with $r_{eff} \sim 0.12$ and 0.57 μm, and black carbon in some cases. The V16 Standard Retrieval mixture is about half nonabsorbing, r_{eff} 0.26 μm spheres and half medium dust.

[44] Caveats to bear in mind regarding the 29 July MISR-AATS comparison include the fact that variability dominates this comparison and that there was no MISR retrieval in exact AATS-coincident pixels because of cloud contamination. It is also noteworthy that V15 and V16 AOD values were fairly similar in pixels near the J31 path, but V16 Ångstrom exponent increases in nearby MISR cells.

[45] A conjecture is that V16 picks up as "dust" an $r_{eff} > 0.26$ μm or nonspherical component. This could be cirrus or a medium spherical particle mixture not in theV16 climatology. A newer version, V19, may yield improvement over V16 by including aerosol mixtures having 100% medium-mode spherical particle mixtures available in V15 but not in V16.

3.3. MODIS-AATS AOD Comparisons

[46] AATS underflew MODIS-Terra and MODIS-Aqua several times in ICARTT. For 3 Terra and 5 Aqua overpasses, MODIS standard aerosol retrievals were made in 61 MODIS grid cells that contained low-altitude, cloud-free AATS flight segments (for Terra: 17 cells on 17 and 22 July and 2 August; for Aqua: 44 cells on 12, 16, 21, and 23 July and 8 August). Table 2 lists coordinates and characteristics of each of these 61 cells, including the cloud percentage and AOD quality flag returned by the MODIS retrieval, the cell's sun glint angle, retrieved AOD(553 nm), and Angstrom exponents for wavelengths less than and greater than 855 nm. We first illustrate the MODIS-AATS compar-

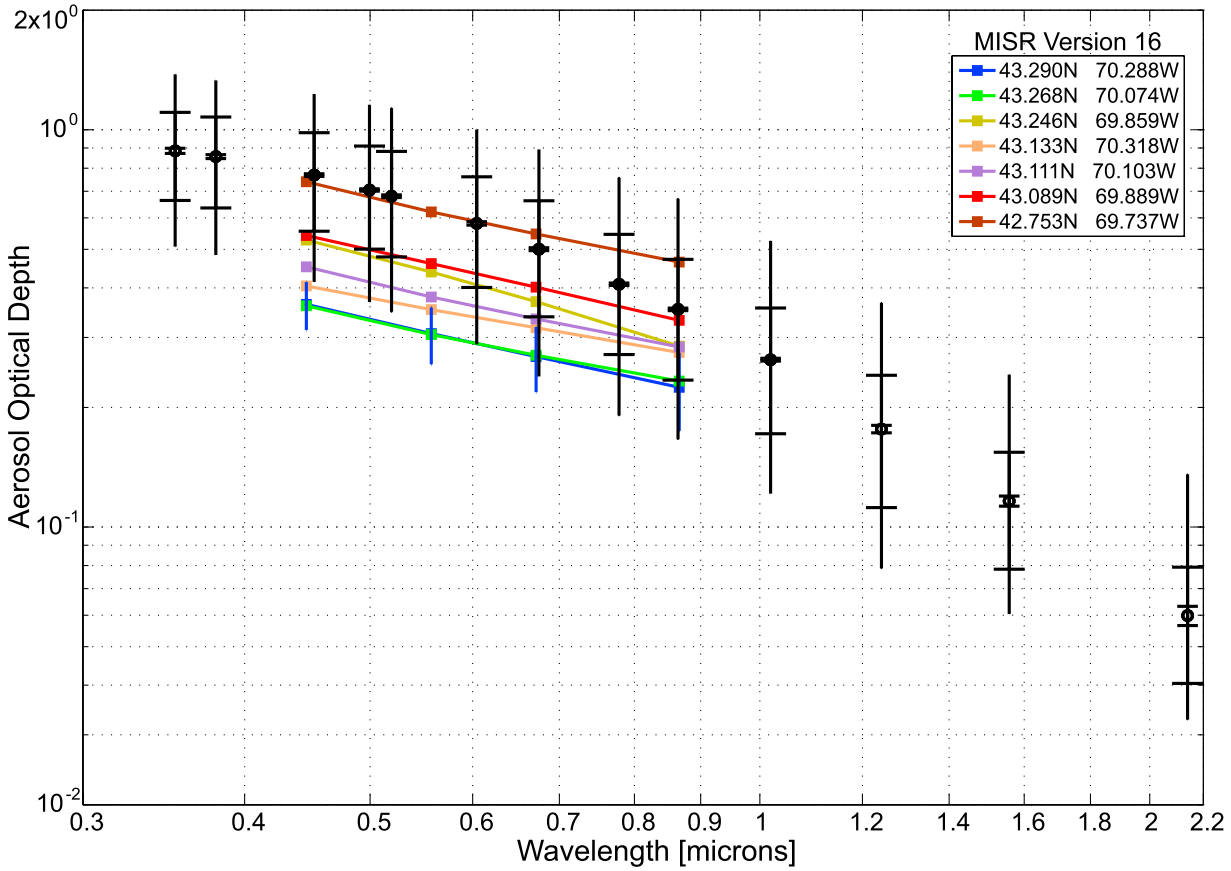

Figure 6. As in Figure 5 but for MISR version 16.

isons by presenting in detail one day, 21 July 2004, and then summarize all the MODIS-AATS comparisons in terms of scatterplots and regression statistics.

[47] All AATS measurements considered in this section were taken within 30 min of satellite overpass time and at J31 altitudes below 100 m, with the following exceptions. For the 12 July Aqua overpass we have included 4 cells with J31 altitude between 100 and 190 m, because the MODIS-AATS comparisons in those cells were virtually identical to that in the single cell with J31 altitude <100 m. For the 16 July Aqua overpass we have included 2 cells with J31 altitude between 100 and 250 m, because the MODIS-AATS comparisons in those cells were virtually identical to that in the single cell with J31 altitude <100 m. For the 2 August Terra overpass we have included 1 cell with J31 measurement time extending to 31 and 33 min after Terra overpass time, because the AATS AOD spectra in those cells were virtually identical to those in the 7 cells with J31 measurements within 30 min of Terra overpass. To assess the effect of including these cells, we report MODIS-AATS comparison statistics with and without them included (see below).

[48] Figure 9 (left) shows the 21 July 2004, 18.10 UT MODIS-Aqua true color image of the New England coastal area in the vicinity of the J31 base (Pease International Tradeport, New Hampshire, near the coast on the Gulf of Maine). Note the grayish haze at the bottom left-middle of the frame, extending northeastward over Cape Cod and toward the Gulf of Maine. The larger-area MODIS image (not shown) reveals that this grayish haze is part of a large smoke plume stretching from Canada into the central United States, then curving E over the coastal Atlantic, N off the mid-Atlantic states and Long Island, and NE into the New England coastal area. The MODIS web site identified the plume as smoke from the Alaska wildfires of 2004, a description consistent with many aircraft measurements in ICARTT [e.g., *Fehsenfeld et al.*, 2006]. Also shown in the MODIS image are the white scattered clouds over land and the larger clouds over the Gulf of Maine, some of which appear grayish (see further discussion below).

[49] Figure 9 (right) shows the J31 flight track for 21 July. Arrows between left and right frames connect coastal features. Figure 10 shows a more detailed view of the J31 track, with 13 grid cells of MODIS aerosol retrievals superimposed.

[50] Figure 11 shows vertical profiles of multiwavelength AOD and extinction from AATS measurements on the initial ascent out of Pease and on spiral descent 1. (See locations of the ascent and descent marked in Figure 10.) As noted in section 2.1, each AATS extinction profile is obtained by vertically differentiating a spline fit to the corresponding AOD profile. Note in the left extinction profile a layer at ~5 km altitude, which is missing in the right extinction profile. Because analyses from other aircraft in the area [e.g., *Fehsenfeld et al.*, 2006] showed the Alaska-Canada smoke to be layered at altitudes ~5 km,

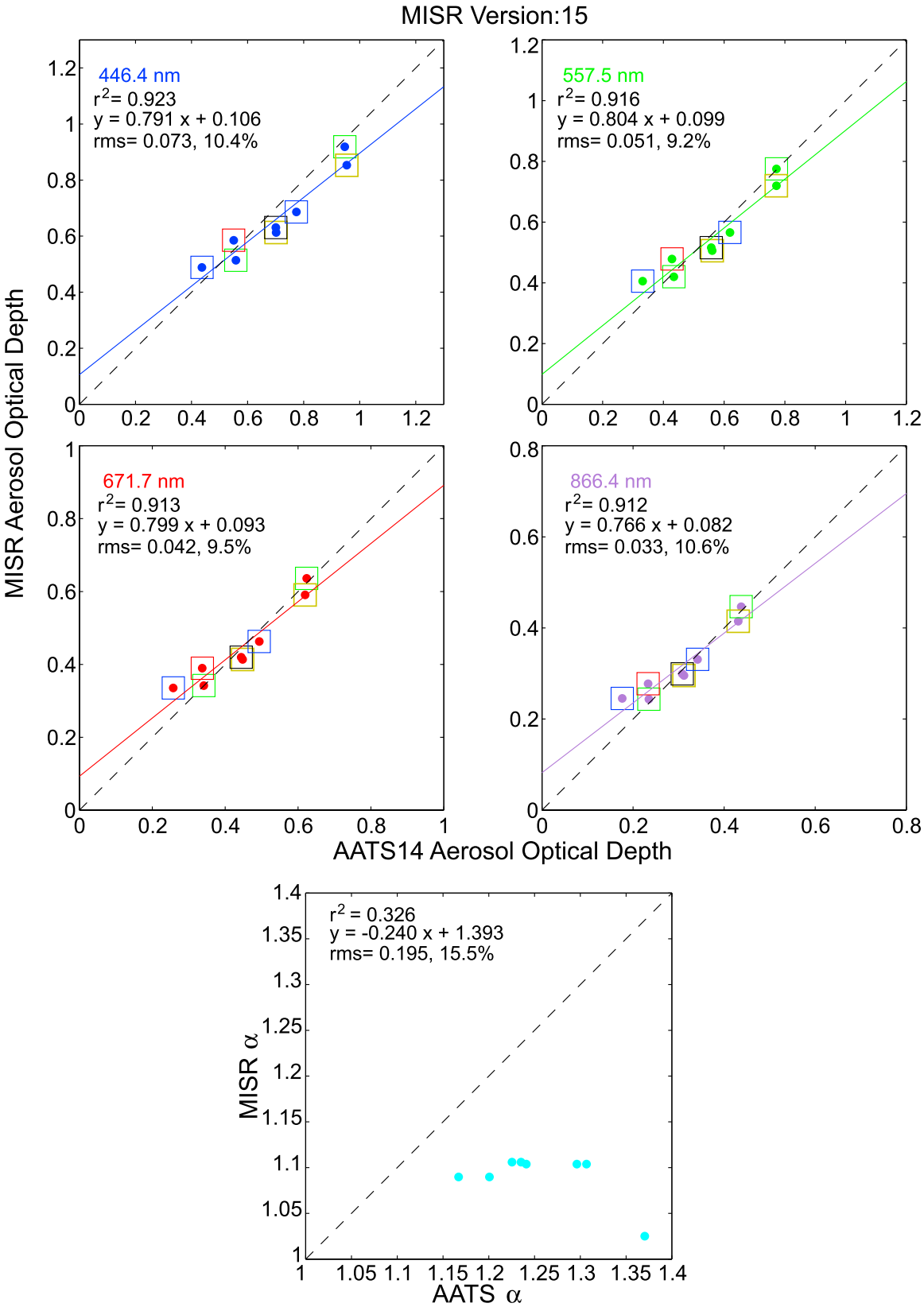

Figure 7. Scatterplots comparing AATS and MISR version 15 AOD and Ångstrom exponent for 29 July 2004.

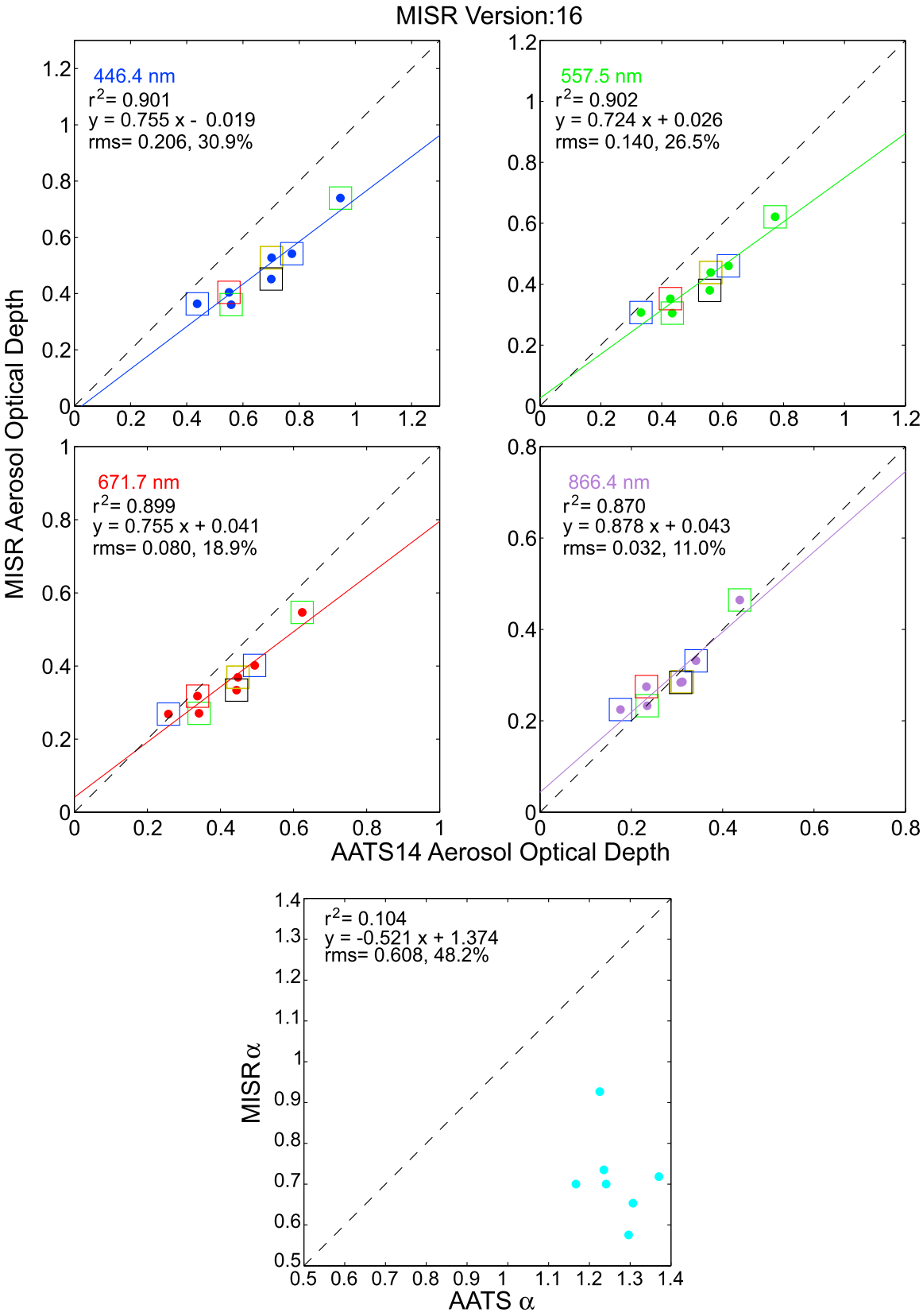

Figure 8. Scatterplots comparing AATS and MISR version 16 AOD and Ångstrom exponent for 29 July 2004.

Table 2. MODIS Cases Using Cells Allowed by the Standard Glint Mask (Glint Angle $\psi > 40°$)

		Overpass Time, UT		Grid Cell Center					AOD(553 nm)		α(553, 855 nm)		α(855, 2119 nm)	
Date, 2004	Satellite	hhmm	Decimal h	Lon W	Lat N	Cloud %	AOD Retrieval Quality Flag[a]	Glint Angle, deg	MODIS	AATS	MODIS	AATS	MODIS	AATS
12 Jul	Aqua	1813	18.22	69.392	43.002	4	3	71.865	0.288	0.254	1.481	1.544	1.932	1.947
12 Jul	Aqua	1813	18.22	69.884	42.965	0	3	69.632	0.333	0.307	1.468	1.530	1.987	2.054
12 Jul	Aqua	1813	18.22	69.408	43.090	24	3	71.896	0.297	0.281	1.462	1.559	1.977	2.017
12 Jul	Aqua	1813	18.22	69.659	43.071	0	3	70.777	0.345	0.324	1.459	1.543	1.950	2.077
12 Jul	Aqua	1813	18.22	69.901	43.053	0	3	69.655	0.318	0.314	1.481	1.531	2.040	2.054
16 Jul	Aqua	1748	17.80	68.538	42.510	35	1	41.933	0.209	0.214	1.595	1.814	0.522	1.582
16 Jul	Aqua	1748	17.80	68.672	42.494	60	1	41.021	0.192	0.212	1.517	1.809	0.580	1.602
16 Jul	Aqua	1748	17.80	68.563	42.598	40	1	41.978	0.214	0.221	1.626	1.783	0.543	1.579
17 Jul	Terra	1513	15.22	70.279	43.098	48	1	68.676	0.078	0.052	1.210	0.830	1.070	−0.100
17 Jul	Terra	1513	15.22	70.299	43.009	30	1	68.659	0.072	0.061	1.150	0.730	1.250	−0.110
17 Jul	Terra	1513	15.22	70.319	42.920	52	1	68.641	0.063	0.072	1.130	0.630	0.910	−0.110
21 Jul	Aqua	1806	18.10	70.458	43.088	53	3	59.781	0.456	0.366	1.433	1.617	1.860	1.856
21 Jul	Aqua	1806	18.10	70.294	43.193	0	3	60.816	0.364	0.314	1.497	1.628	2.106	1.767
21 Jul	Aqua	1806	18.10	69.934	43.317	0	3	62.891	0.313	0.274	1.501	1.630	2.119	1.729
21 Jul	Aqua	1806	18.10	70.128	43.300	0	3	61.867	0.315	0.275	1.506	1.630	2.142	1.735
21 Jul	Aqua	1806	18.10	70.317	43.283	0	3	60.847	0.338	0.272	1.484	1.624	2.132	1.694
21 Jul	Aqua	1806	18.10	69.756	43.423	8	3	63.948	0.311	0.265	1.507	1.637	2.141	1.714
21 Jul	Aqua	1806	18.10	69.955	43.406	0	3	62.914	0.304	0.265	1.500	1.635	2.119	1.716
21 Jul	Aqua	1806	18.10	70.149	43.388	0	3	61.881	0.316	0.264	1.477	1.626	2.106	1.691
21 Jul	Aqua	1806	18.10	69.573	43.531	14	3	65.011	0.285	0.251	1.597	1.634	1.453	1.700
21 Jul	Aqua	1806	18.10	69.778	43.513	0	3	63.965	0.298	0.253	1.512	1.635	2.161	1.695
21 Jul	Aqua	1806	18.10	69.977	43.495	0	3	62.939	0.303	0.261	1.506	1.636	2.145	1.696
21 Jul	Aqua	1806	18.10	70.171	43.478	0	1	61.907	0.294	0.266	1.540	1.635	1.816	1.700
21 Jul	Aqua	1806	18.10	69.798	43.601	0	3	63.997	0.302	0.255	1.489	1.629	2.150	1.703
22 Jul	Terra	1531	15.52	69.975	42.992	0	1	40.159	0.380	0.457	1.838	1.585	2.677	1.969
22 Jul	Terra	1531	15.52	70.131	42.920	0	1	41.005	0.380	0.447	1.779	1.600	2.313	1.920
22 Jul	Terra	1531	15.52	70.001	42.903	0	1	40.115	0.380	0.444	1.701	1.595	1.969	1.956
22 Jul	Terra	1531	15.52	70.158	42.831	0	1	40.972	0.386	0.456	1.767	1.601	2.258	1.956
22 Jul	Terra	1531	15.52	70.028	42.815	0	1	40.072	0.475	0.449	1.599	1.593	2.682	1.958
23 Jul	Aqua	1754	17.90	69.998	42.770	0	3	43.770	0.481	0.508	1.469	1.567	1.837	2.141
23 Jul	Aqua	1754	17.90	70.023	42.858	0	3	43.803	0.571	0.572	1.443	1.574	1.888	2.170
23 Jul	Aqua	1754	17.90	70.049	42.947	12	3	43.843	0.573	0.538	1.435	1.597	1.860	2.153
23 Jul	Aqua	1754	17.90	70.238	43.108	8	3	43.032	0.565	0.670	1.458	1.608	1.484	2.145
23 Jul	Aqua	1754	17.90	70.373	43.092	0	3	42.135	0.534	0.616	1.516	1.632	1.676	2.118
23 Jul	Aqua	1754	17.90	70.126	43.213	20	3	43.957	0.597	0.656	1.459	1.605	1.610	2.164
23 Jul	Aqua	1754	17.90	70.263	43.196	0	3	43.066	0.572	0.658	1.476	1.606	1.670	2.155
2 Aug	Terra	1513	15.22	70.274	43.140	17	1	70.468	0.216	0.213	1.376	1.538	1.500	1.608
2 Aug	Terra	1513	15.22	70.294	43.051	0	1	70.452	0.198	0.183	1.273	1.562	1.648	1.505
2 Aug	Terra	1513	15.22	70.080	43.033	0	1	69.382	0.192	0.175	1.287	1.564	1.712	1.473
2 Aug	Terra	1513	15.22	70.313	42.962	0	1	70.427	0.179	0.175	1.294	1.576	1.744	1.470
2 Aug	Terra	1513	15.22	70.099	43.944	0	1	69.365	0.181	0.169	1.323	1.573	1.547	1.437
2 Aug	Terra	1513	15.22	70.120	42.855	0	1	69.350	0.176	0.159	1.355	1.617	1.671	1.407
2 Aug	Terra	1513	15.22	69.912	42.837	0	1	68.299	0.187	0.160	1.348	1.610	1.645	1.380
2 Aug	Terra	1513	15.22	69.932	42.748	0	1	68.270	0.205	0.194	1.372	1.654	1.721	1.516
2 Aug	Terra	1513	15.22	69.730	42.730	0	1	67.233	0.240	0.236	1.491	1.643	1.612	1.623
8 Aug	Aqua	1754	17.90	68.105	42.779	0	1	57.525	0.066	0.062	1.936	1.452	1.528	0.590
8 Aug	Aqua	1754	17.90	68.267	42.762	0	1	53.587	0.068	0.065	1.975	1.483	1.559	0.616
8 Aug	Aqua	1754	17.90	68.426	42.746	4	1	55.651	0.051	0.063	2.238	1.500	1.200	0.597
8 Aug	Aqua	1754	17.90	68.582	42.729	6	1	54.711	0.045	0.054	2.494	1.450	1.752	0.506
8 Aug	Aqua	1754	17.90	68.735	42.713	4	1	53.792	0.043	0.051	2.646	1.423	2.351	0.466
8 Aug	Aqua	1754	17.90	68.760	42.802	7	1	53.826	0.039	0.052	2.517	1.409	1.822	0.462
8 Aug	Aqua	1754	17.90	68.912	42.786	21	1	52.912	0.036	0.049	2.753	1.432	3.210	0.446
8 Aug	Aqua	1754	17.90	69.060	42.769	6	1	51.989	0.038	0.046	2.652	1.446	2.393	0.417
8 Aug	Aqua	1754	17.90	69.207	42.753	1	1	51.088	0.039	0.045	2.322	1.451	1.346	0.418
8 Aug	Aqua	1754	17.90	69.351	42.736	0	1	50.185	0.039	0.047	2.433	1.461	1.587	0.481
8 Aug	Aqua	1754	17.90	69.494	42.720	0	1	49.301	0.041	0.046	2.171	1.455	1.098	0.461
8 Aug	Aqua	1754	17.90	69.634	42.704	0	1	48.412	0.042	0.043	2.260	1.470	1.235	0.404
8 Aug	Aqua	1754	17.90	69.659	42.792	0	1	48.446	0.041	0.044	2.418	1.454	1.550	0.441
8 Aug	Aqua	1754	17.90	69.798	42.776	0	1	47.570	0.034	0.042	2.753	1.463	3.210	0.396
8 Aug	Aqua	1754	17.90	69.935	42.760	1	1	46.690	0.030	0.043	2.753	1.469	3.210	0.399
8 Aug	Aqua	1754	17.90	70.071	42.743	6	1	45.834	0.029	0.044	2.753	1.441	3.210	0.385

[a]0, no confidence; 1, marginal; 2, good; 3, very good.

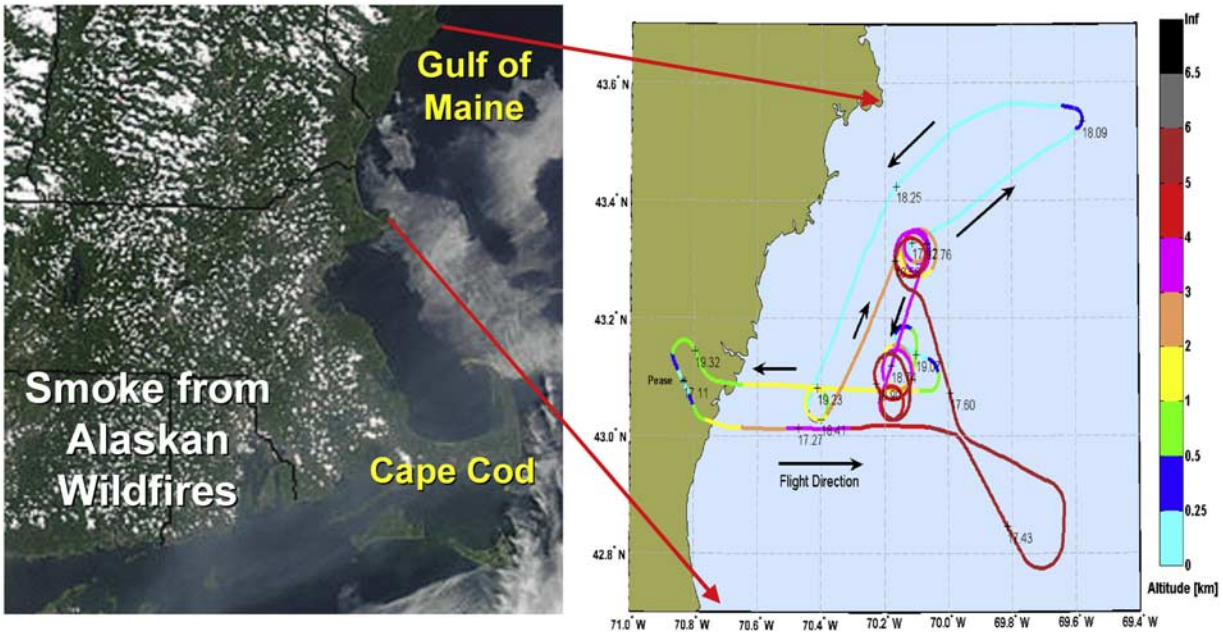

Figure 9. (left) MODIS Aqua image, 21 July 2004, 1805 UT. (right) J31 flight track.

we identify the extinction layer at ~5 km as being from this smoke, which was evidently present at the location of initial ascent, but not at spiral descent 1 (see Figures 9 and 10).

[51] Figure 12 shows a detailed view of the low-altitude J31 flight path and the 13 MODIS grid cells along it, together with time series of J31 altitude and AATS-measured AOD. Colored vertical lines on the AOD versus time plot show edges of MODIS grid cells, and colored horizontal arrows span the time segment the J31 spent in each grid cell. Note the increase in AOD during 18.30–

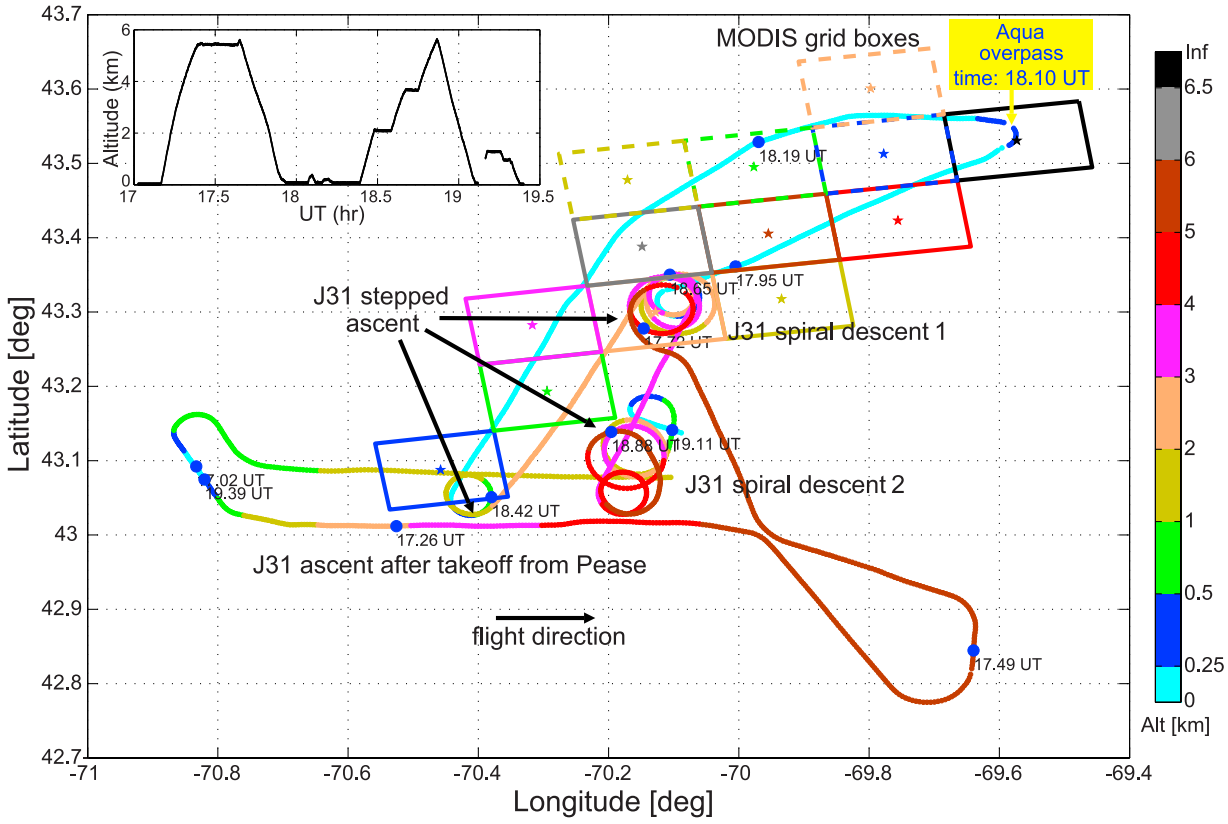

Figure 10. J31 flight path on 21 July 2004, with MODIS grid cells superimposed on path parts at minimum altitude (<100 m ASL).

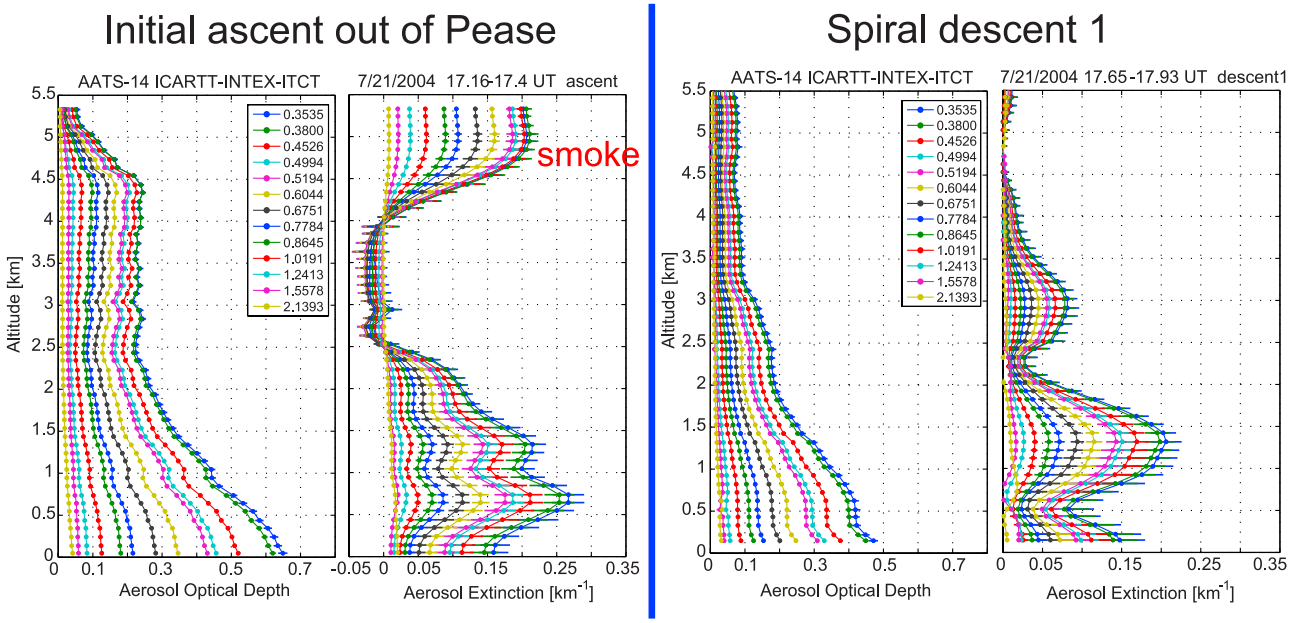

Figure 11. Vertical profiles of AOD and extinction from AATS measurements on the J31. (left) From initial ascent out of Pease. (right) From spiral descent 1.

18.37 UT, when the J31 flew from the pink MODIS cell, into and across the green cell, and into the blue cell. This AOD increase occurs as the J31 flies toward the location of the ascent out Pease (which had the extinction layer at ~5 km altitude, Figure 11) and away from the location of spiral descent 1 (which was missing this layer). Thus the most likely reason for the AOD increase is that the J31 is flying into the region covered by the elevated smoke plume. *Redemann et al.* [2006b] explore the impacts of this and other AOD gradients on radiative fluxes, deriving radiative forcing efficiencies.

[52] Figure 13 compares AOD spectra from the 13 MODIS grid cells in Figures 10 and 12 with the AOD spectrum from AATS averaged along the flight path. Also shown are the AATS AOD uncertainty (narrow ticks), standard deviation along the flight path (wide ticks), and

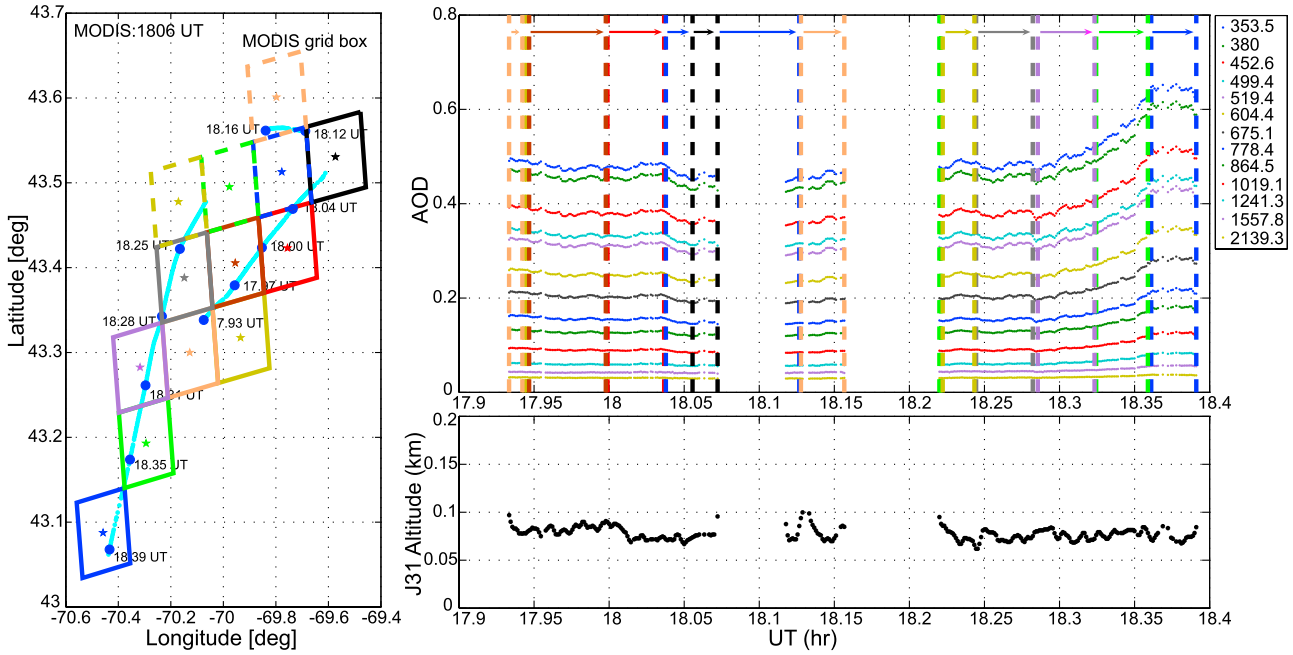

Figure 12. (left) Detail of J31 flight path on 21 July 2004, showing MODIS grid cells. (right) AOD and J31 altitude versus time along the flight path at left. Vertical lines in top right frame show edges of MODIS grid cells.

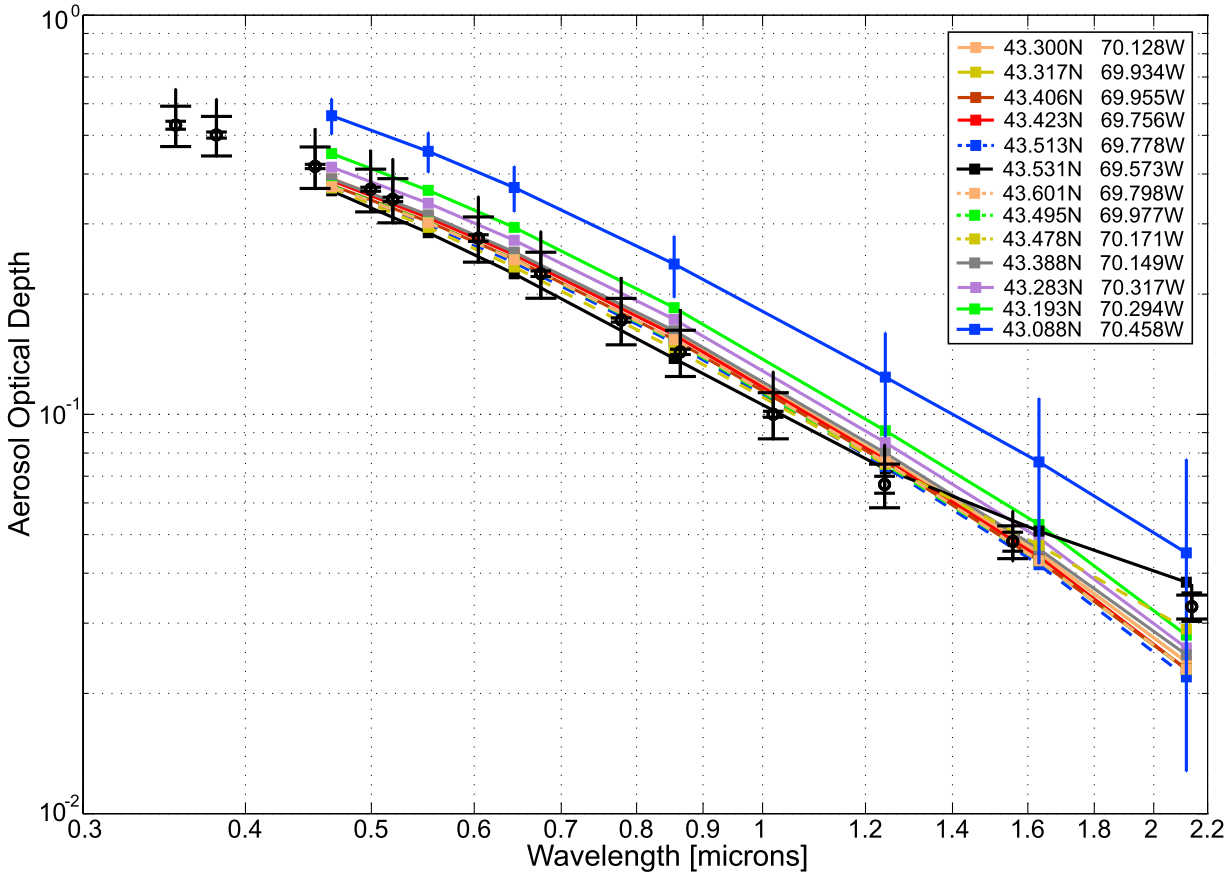

Figure 13. Comparison of AOD spectra from J31 and MODIS within the grid cells shown in Figure 12.

range (vertical bars with no ticks). AATS AOD spectra from the 13 individual MODIS cells are shown in Figure 14, each compared to the corresponding MODIS AOD spectrum.

[53] Note that the MODIS retrievals in Figure 13 show an AOD gradient with the sign of the AATS AOD gradient (i.e., MODIS AOD increases in going from pink cell to green to blue), but that the blue-cell MODIS AODs exceed the AATS AODs by more than the combined uncertainties at wavelengths 553–1243 nm. Our analyses suggest that the large MODIS AODs in the blue cell are caused by cloud contamination, which is enabled by smoke over cloud impairing the MODIS cloud mask. Following is the evidence on which we base this conjecture. First we note the heights of the smoke (∼5 km, per Figure 11 and associated discussion above) and clouds (880 hPa or ∼1.2 km, per the MODIS cloud product, which showed clouds in the blue cell as scattered and broken). Hence the smoke was definitely above the clouds. The presence of clouds in the cell is also consistent with the gaps in the AATS AOD traces, 18.36–18.38 UT in Figure 12 (also indicated by gaps in the J31 flight track in the blue cell). These gaps are caused by clouds intermittently blocking the AATS-to-Sun viewing path. As noted in section 2.1, the AATS processing algorithm detects these clouds via their effect on the time variation of AATS detector signals (specifically the standard deviation of detector output voltages measured at 3 Hz over a 3-s period). It then excludes such signals from AOD analysis. As noted in section 2.3.1, the MODIS cloud screen uses the standard deviation of 553 nm reflectances in groups of 3 by 3 pixels [*Remer et al.*, 2005; *Martins et al.*, 2002]. Smoke, a moderately absorbing aerosol, is expected to reduce column reflectance over cloud (a bright surface) and increase it over cloud-free ocean pixels (by virtue of the small surface albedo there). Such reflectance changes will reduce the standard deviation of MODIS 553 nm reflectance in 3-by-3 pixel groups that are partly cloud and partly ocean. Partly cloudy pixel groups which, in the absence of smoke, have standard deviation just above the cloud threshold of 0.0025 could have their standard deviation reduced by the smoke, and hence escape detection. Inclusion of such pixel groups in the AOD retrieval would artificially increase AOD values.

[54] Additional evidence for this process is given by the MODIS grid cell cloud fractions and Ångstrom exponent values. Of the 13 cells for 21 July in Table 2 and in Figures 10, 12, and 14, all but 3 report "no clouds" and use all the available pixels to make the retrieval. The three exceptions are the blue cell (centered at 43.088°N), which reports 53% clouds, and two cells at the opposite end of the group, i.e., the red cell (centered at 43.423°N), which reports 8% clouds, and the black cell (centered at 43.531°N), which reports 14% clouds (see also Table 2). In other words, in a nearly cloud-free set of 13 cells, the blue cell reports the largest cloud fraction, 53%. Smoke over the clouds in such a cell could very well smooth out the reflectance variability of the clouds, as explained above.

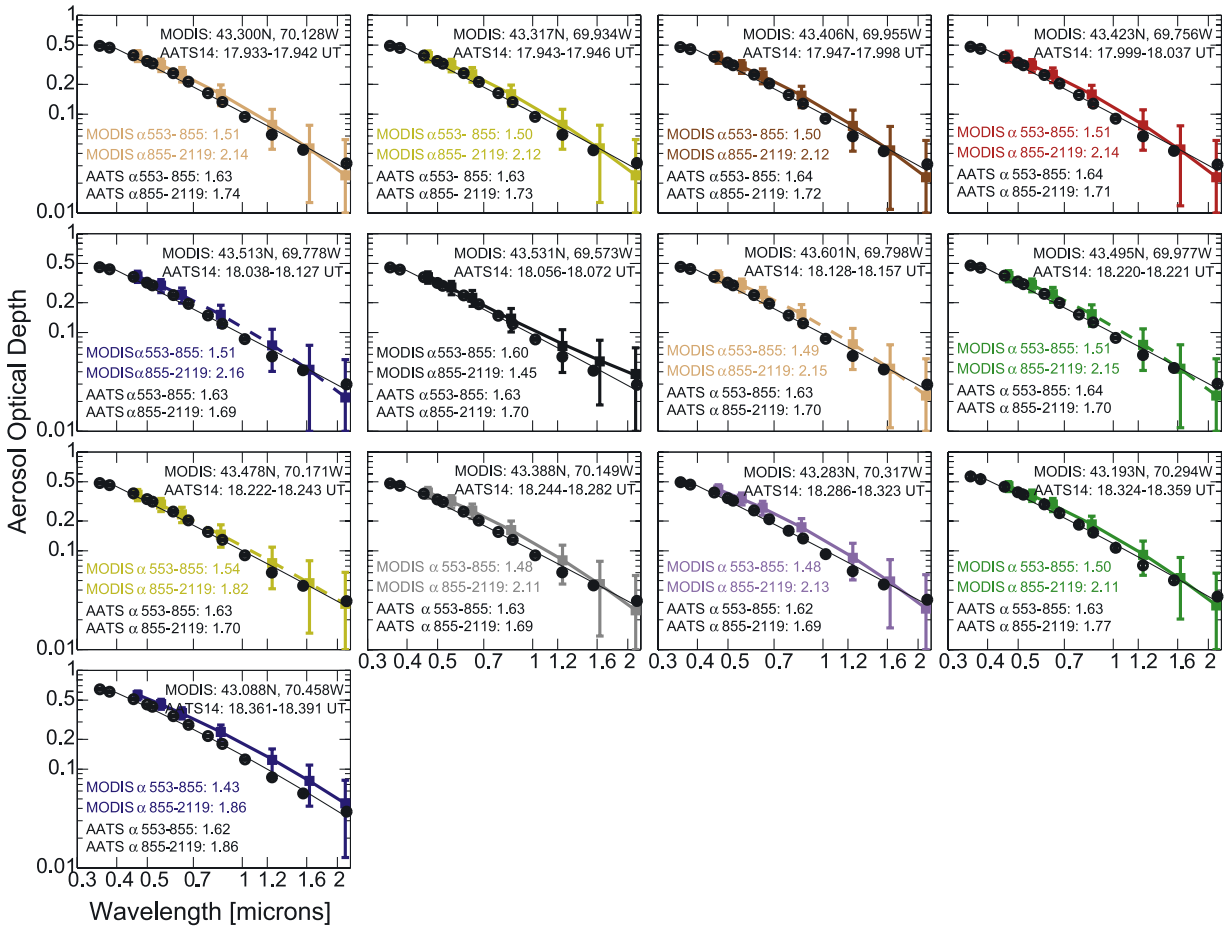

Figure 14. Comparisons of MODIS and AATS AOD-versus-wavelength spectra for each of the 13 MODIS grid cells along the 21 July 2004 J31 path shown in Figure 12.

Another possibility is clouds scattering light from or out of the sides of clouds, a situation previously analyzed by *Wen et al.* [2006] and *Nikolaeva et al.* [2005].

[55] Regarding MODIS Ångstrom exponent values, notice in Figure 14 that they decrease in going from the pink and green cells to the blue cell. This is true for both wavelength ranges, 553–855 nm and 855–2119 nm, but especially so for the longer wavelength range, which would be most affected by reflectance from cloud particles. Specifically, for 855–2119 nm, the MODIS Ångstrom exponent in the blue cell, 1.86, is 12% less than the average value in the pink and green cells, 2.12;. In contrast, the AATS Ångstrom exponent for 855–2119 nm in the blue cell, 1.86, is actually 7% larger than the red-green average of 1.73, possibly caused by the elevated smoke plume having smaller particles than the haze below. Because the cell-to-cell differences in MODIS Ångstrom exponent described here are relatively small (i.e., 0.26), they may not be significant enough to constitute proof of cloud contamination, but they are consistent with cloud contamination and do provide supporting evidence. See also section 3.4.

[56] Note also the data-quality flags in Table 2 for each of the 13 cells of 21 July. Twelve of the 13 cells have QA = 3 (indicating high data quality), including the 3 squares mentioned above with some cloud fraction. There is one square with QA = 1 (low quality) because it had some difficulty fitting a model. This is the cell centered at 43.478°N, but its AOD spectrum is very similar to its neighbors, and there is no reason to eliminate it.

[57] In an effort to further quantify our analysis of possible cloud effects on MODIS retrieved AOD values for the 21 July case, we have studied effects of varying the threshold for cloud detection (i.e., the standard deviation of 553-nm reflectances in 3 × 3 groups of pixels, described above). We first reduced the threshold from its standard value, 0.0025, to 0.0020. This had a notable effect on AOD retrievals in a band just east of the J31 low-altitude transect. Specifically, this band, which appeared like cloud covered by smoke in MODIS true-color imagery (just east of that shown in Figure 9) produced AOD retrievals with AOD(553 nm) ~1 when threshold was set to 0.0025; however, when threshold was reduced to 0.0020, many cells that had previously returned AOD values became classified as cloud and gave no AOD retrieval. Further reductions of the threshold in this band caused corresponding reductions in the number of cells returning AOD values, until all were eliminated when threshold = 0.0005. These same reductions in threshold caused essentially no effect on MODIS AOD returned for cells along the J31 low-

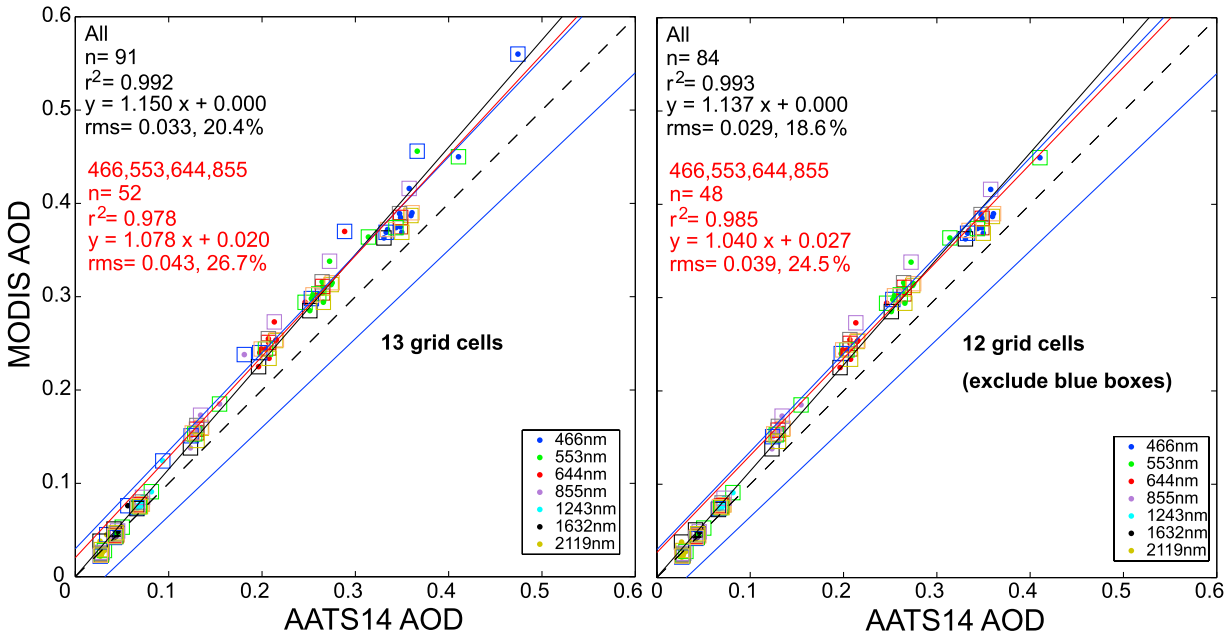

Figure 15. Scatterplots comparing AATS and MODIS-Aqua AOD for the 21 July 2004 case. Blue lines show the MODIS over-ocean uncertainty estimates, $\Delta\tau = \pm 0.03 \pm 0.05\tau$. (left) Including all 13 grid cells. (right) Excluding the blue grid cell in Figure 12 (blue spectrum in Figure 13), data points for which were indicated in the left frame with blue boxes.

altitude path (including the blue cell in Figures 10 and 12–14), but they increased the reported cloud fraction in the blue cell from 54% at threshold = 0.0025 to 88% at threshold = 0.0004. Finally, reducing threshold to 0.00025 (one tenth the standard value) caused the blue cell to become classified as cloud (returning no AOD value) while the other cells along the J31 low-altitude path continued to yield AOD values very similar to those shown in Figures 13 and 14.

[58] From these analyses we conclude that smoke above cloud can indeed impair the MODIS cloud mask by reducing the standard deviation of 3 × 3 pixel groups, causing some cloudy cells to yield retrieved AOD values that are greater than the true AOD in those cells. Reducing the threshold for cloud detection can eliminate some such cells, but it is currently not clear what threshold value is appropriate. Moreover, in partly cloudy cells (like the blue cell on 21 July), severe threshold reductions may be required to eliminate AOD retrievals that have possible cloud effects, and such threshold reductions may eliminate the AOD retrieval altogether (while having negligible effect on cloud-free cells). Furthermore, the consequences of light scattering from or out of cloud sides (mentioned above) must be explored before cases like this can be fully understood. Finally, because the J31 was in the blue cell 15 to 20 min after MODIS overpass (at 1806 UT), it is also possible that the smoke plume covering most or all of the blue cell at 1806 UT had moved to cover less or none of it 15 min later. In spite of these remaining questions, we feel that this case is very instructive and points the way to future studies to resolve those questions.

[59] Figure 15 presents scatterplots comparing MODIS and AATS AODs for the 21 July case. Also shown are the MODIS uncertainty estimates of $\Delta\tau = \pm 0.03 \pm 0.05\tau$ as blue lines. As with the MISR-AATS comparisons, AATS AODs for each grid cell were obtained by averaging all AATS measurements within the cell to yield a spectrum of ln AOD versus ln λ, which was then fitted with a quadratic least squares fit (exemplified by the thin black curves in Figure 14). From the AATS-derived fit, the AOD at the intermediate MODIS wavelengths of 466, 553, 644, 855, 1243, 1632 and 2119 nm was determined. Although several MODIS wavelengths are close to AATS-14 wavelengths (see Figure 14), the fit procedure above was used to

Table 3. Statistics[a] of MODIS-AATS Comparisons for 21 July 2004

Case	a	b	R^2	RMS Difference	N
13 cells, all 7 MODIS 1 λ	1.150	0.000	0.99	0.033, 20.4%	91
12 cells,[b] all 7 MODIS 1 λ	1.137	0.000	0.99	0.029, 18.6%	84
13 cells, 466, 553, 644, 855 nm	1.078	0.020	0.98	0.043, 26.7%	52
12 cells,[b] 466, 553, 644, 855 nm	1.040	0.027	0.99	0.039, 24.5%	48

[a]a and b, coefficients of equation AOD(satellite) = a × AOD(AATS) + b; R^2, correlation coefficient squared; N, number of points regressed (cells × wavelengths).
[b]Excludes blue cell in Figures 10 and 12–14.

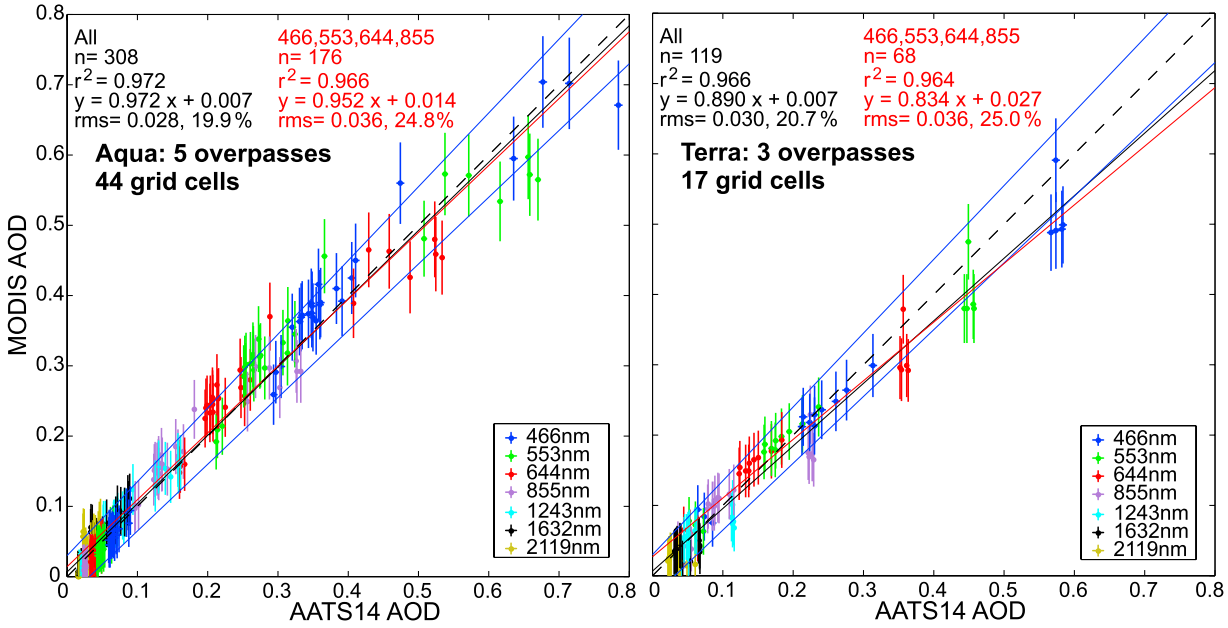

Figure 16. Scatterplots comparing AATS and MODIS AOD for all coincidences with good data in INTEX-ICARTT 2004. Blue lines show the MODIS over-ocean uncertainty estimates, $\Delta\tau = \pm 0.03 \pm 0.05\tau$. (left) MODIS-Aqua versus AATS. (right) MODIS-Terra versus AATS.

minimize the impact of possible AATS-14 single-channel contamination, calibration uncertainties and uncertainties stemming from gaseous absorption in the AATS channels, the latter being particularly important at the near-IR wavelengths.

[60] The plot on the left in Figure 15 includes all 13 MODIS grid cells, whereas the plot on the right excludes the blue cell that is suspected of cloud contamination. Table 3 summarizes the regression statistics for these scatterplots. Comparing the cases with and without the blue cell shows how excluding the blue cell reduces the RMS difference between MODIS and AATS results (from 0.033 to 0.029, or from 20.4% to 18.6%), and increases R^2 (though negligibly, from 0.992 to 0.993). The percentage of MODIS AOD retrievals within $\Delta\tau = \pm 0.03 \pm 0.05\tau$ of the AATS values increases from 80% to 83% when the blue cell is excluded; the fraction of near-IR retrievals (855–2119 nm) increases from 96 to 98%.

[61] As mentioned above, in ICARTT there were 61 MODIS standard aerosol retrieval grid cells that (1) produced MODIS AOD spectra and (2) contained J31 low-altitude flight segments that provided AATS AOD values (17 cells from 3 Terra overpasses, and 44 cells from 5 Aqua overpasses). Figure 16 presents scatterplots comparing MODIS and AATS AODs for these 61 cases (including the 21 July MODIS-Aqua cell suspected of cloud contamination), separated into Aqua and Terra cases. The MODIS and AATS AOD uncertainties are also shown as error bars on each data point. About 87% of the MODIS AOD retrievals differ from AATS AODs by less than the pre-

Table 4. Statistics[a] of MODIS-AATS Comparisons for All Overpasses With MODIS AOD Retrievals Allowed by the Standard Glint Mask (Glint Angle y > 40°)

Case	a	b	R^2	RMS Difference	N
Aqua, 44 cells, all 7 MODIS 1 λ	0.972	0.007	0.97	0.028, 19.9%	308
Aqua, 38 cells,[b] all 7 MODIS 1 λ	0.969	0.006	0.97	0.030, 21.3%	266
Terra, 17 cells, all 7 MODIS 1 λ	0.890	0.007	0.97	0.030, 20.7%	119
Terra, 16 cells,[c] all 7 MODIS 1 λ	0.888	0.006	0.97	0.031, 21.3%	112
Aqua, 44 cells, 466, 553, 644, 855 nm	0.952	0.014	0.97	0.036, 24.8%	176
Aqua, 38 cells,[b] 466, 553, 644, 855 nm	0.948	0.014	0.97	0.038, 27.1%	152
Terra, 17 cells, 466, 553, 644, 855 nm	0.834	0.027	0.96	0.036, 25.0%	68
Terra, 16 cells,[c] 466, 553, 644, 855 nm	0.833	0.027	0.96	0.037, 25.7%	64
Aqua, 44 cells, 855 nm	1.038	0.001	0.95	0.024, 19.5%	44
Aqua, 38 cells,[b] 855 nm	1.035	−0.002	0.95	0.025, 20.9%	38
Terra, 17 cells, 855 nm	0.696	0.032	0.87	0.029, 23.3%	17
Terra, 16 cells,[c] 855 nm	0.696	0.031	0.87	0.030, 24.1%	64

[a]a and b, coefficients of equation AOD(satellite) = a × AOD(AATS) + b; R^2, correlation coefficient squared; N, number of points regressed (cells × wavelengths).
[b]Excludes 4 cells on 12 July with AATS altitude 100 to 190 m and 2 cells on 16 July with AATS altitude 100–250 m.
[c]Excludes 1 cell on 2 August with AATS measurement time 31–33 min after Terra overpass time.

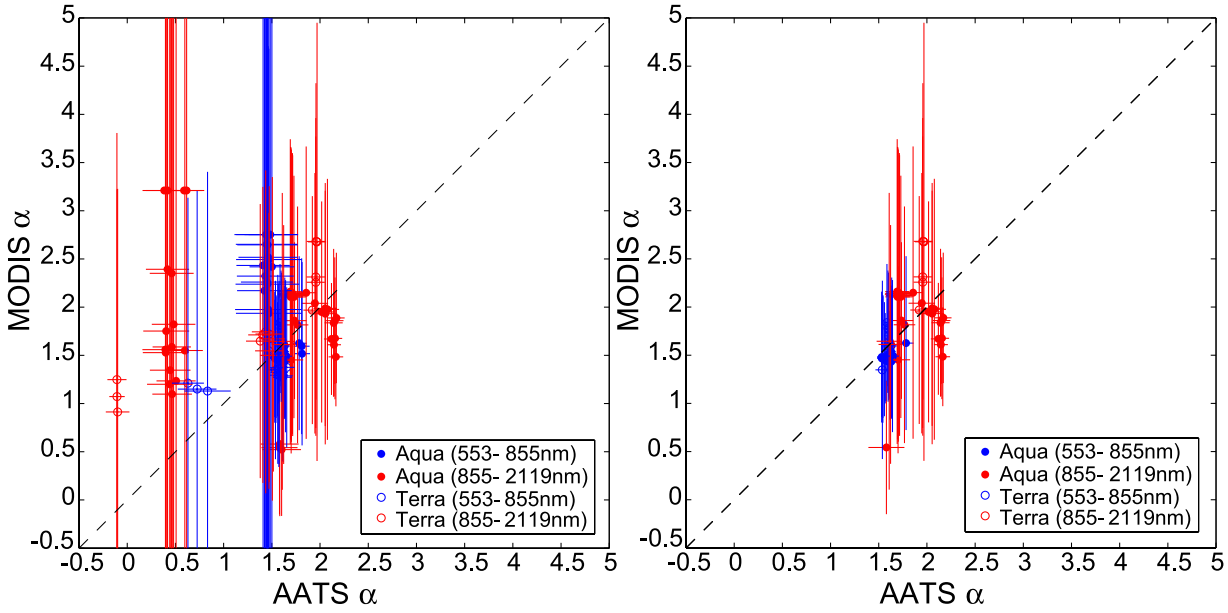

Figure 17. Scatterplot comparisons of 553–855 nm (blue symbols) and 855–2119 nm (red symbols) Ångstrom exponents for MODIS-Terra and MODIS-Aqua versus AATS-14 derived Ångstrom exponents. (left) All 40 Aqua and 17 Terra cases. (right) Excluding all cases with AATS AOD(855) < 0.1.

dicted MODIS over-ocean uncertainty, $\Delta\tau = \pm 0.03 \pm 0.05\tau$; the fraction of near-IR retrievals that fall within this uncertainty range is about 93%. Table 4 summarizes statistics for the scatterplots in Figure 16. When all MODIS wavelengths are included, RMS MODIS-AATS AOD differences are 0.028 (20%) for MODIS-Aqua and 0.030 (21%) for MODIS-Terra. When wavelengths are restricted to 466, 553, 644, and 855 nm, the RMS AOD differences become 0.036 (25%) for MODIS-Aqua and 0.036 (25%) for MODIS-Terra. R^2 values for all 4 cases are between 0.964 and 0.972.

[62] Table 4 also shows statistics obtained when repeating the comparisons and excluding the 7 MODIS cells described above that did not quite meet our criteria of AATS altitude <100 m and AATS measurement time within 30 min of satellite overpass time. Comparing the statistics obtained when including or excluding those cells (e.g., in Table 4, Aqua, 44 cells versus Aqua, 38 cells, and Terra, 17 cells versus Terra, 16 cells) shows that excluding the cells produces essentially no change in comparison statistics.

[63] It is striking that the good MODIS-AATS AOD agreement described above and shown in Figure 16 and Table 4 is achieved even though the AOD retrieval quality flag (see Table 2) is 1 (marginal) for 37 of the 61 cases (with the remaining 24 cases rated 3 (very good)). Some of the conditions for reducing the quality flag from 3 to 1 are conservative. In the present cases, they include (1) fitting error (i.e., differences between measured and retrieval model reflectances) exceeding a critical value and (2) one channel (e.g., 1632 nm on Aqua) appearing faulty, which is not as crucial as the minimum number of cloud-free pixels, the presence of glint or the absence of both the 1632 and 2119 nm channels. The good MODIS-AATS agreement found for these over-ocean cases even when the quality flag = 1 (marginal) suggests that it might be possible to relax one or more criteria for setting the quality flag.

3.4. MODIS-AATS Ångstrom Exponent Comparisons

[64] Similar to the methodology used for the AOD comparisons in the previous section, we determined Ångstrom exponents from the AATS-14 measurements within each MODIS retrieval cell by first averaging all cloud-free, low-altitude AATS-14 AOD measurements in the cell, then fitting the spectrum of lnAOD versus lnλ with a quadratic, and finally calculating the Ångstrom exponents from the ratios of the fitted AOD values, τ_{fit}, at the respective wavelengths, i.e.,

$$\alpha = -\frac{\ln\left[\tau_{fit}(\lambda_1)/\tau_{fit}(\lambda_2)\right]}{\ln(\lambda_1/\lambda_2)} \quad (3)$$

where the wavelength pairs are 553 and 855 nm for the first and 855 and 2119 nm for the second Ångstrom exponent, respectively.

[65] Figure 17 (left) shows a scatterplot comparison of Ångstrom exponents for 553–855 nm and 855–2119 nm for MODIS-Terra and MODIS-Aqua. In general there is very poor agreement between the Ångstrom exponents from AATS-14 and MODIS. In most cells the MODIS-derived Ångstrom exponents exceed the AATS-derived values, for both 553–855 nm and 855–2119 nm. This is especially so when AATS α(855–2119) < ~1 or when AATS α(553–855) < ~1.6. The RMS differences between AATS-14 and MODIS-derived 553–855 nm Ångstrom exponents are 0.28 (21%) for MODIS-Terra and 0.66 (43%) for MODIS-Aqua; the RMS differences between AATS-14 and MODIS-derived 855–2119 nm Ångstrom exponents are 0.61 (45%) for MODIS-Terra and 1.18 (92%) for MODIS-Aqua. None of the four correlation coefficients has $R^2 > 0.7$.

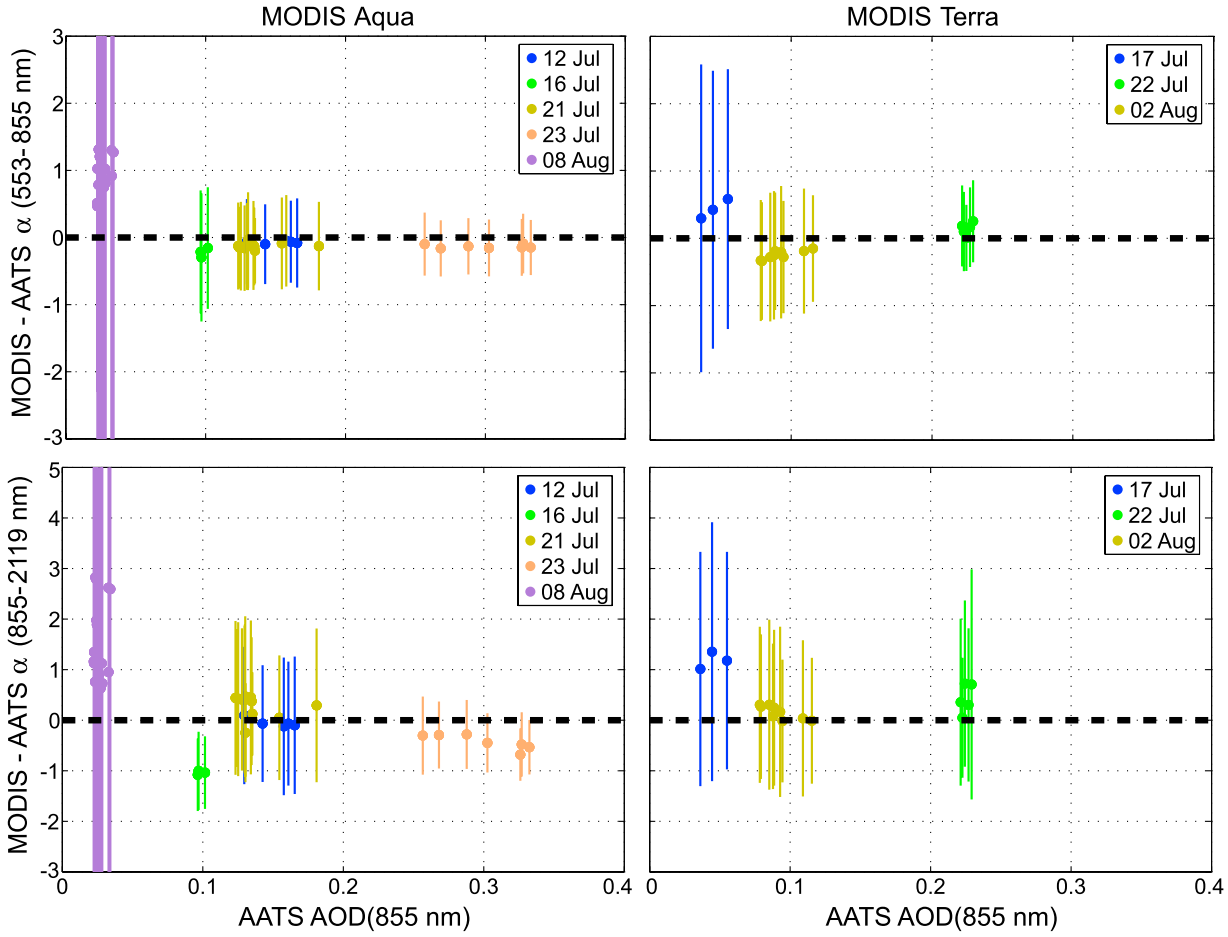

Figure 18. MODIS-AATS differences in Ångstrom exponents plotted versus AATS AOD(855 nm).

[66] Many of the above results for MODIS-AATS Ångstrom comparisons are quite similar to those reported by *Redemann et al.* [2006b] for measurements off the U.S. west coast in April 2004. At first the large differences between AATS and MODIS Ångstrom exponents may seem surprising given the very small differences between AATS and MODIS AOD values (see Figure 16, RMS differences $<\sim$0.04 (19% to 26%)). However, one must bear in mind that the uncertainty in an Ångstrom exponent depends directly on the relative uncertainties in the associated AOD values, which increase as AOD decreases. Specifically, applying standard error propagation analyses [e.g., *Bevington*, 1969] to equation (3) and neglecting correlations between errors at λ_1 and λ_2 yields

$$(\Delta\alpha)^2 = -\frac{[\Delta\tau(\lambda_1)/\tau(\lambda_1)]^2 + [\Delta\tau(\lambda_2)/\tau(\lambda_2)]^2}{[\ln(\lambda_1/\lambda_2)]^2} \qquad (4)$$

where $\Delta\alpha$ is the uncertainty in Ångstrom exponent α. The error bars shown in Figure 17 were calculated using equation (4).

[67] Although most of the AOD points in Figure 16 fall within the MODIS over-ocean uncertainty estimates of $\Delta\tau = \pm 0.03 \pm 0.05\tau$, many AOD values are <0.1, with MODIS AOD uncertainties of 30% to 100% or more. These large AOD relative uncertainties propagate to large Ångstrom absolute uncertainties, as shown in Figure 17 and previously noted by *McArthur et al.* [2003]. This is illustrated further by Figure 18, which shows MODIS-AATS Ångstrom exponent differences as a function of AATS AOD. Note that the largest differences are associated with the smallest AOD values.

[68] Figure 19 shows more explicitly how AOD values can agree within error bars for all wavelengths and still produce Ångstrom exponents that differ by 1 to 2 or more if the relative error bars for AOD are large enough. The AATS and MODIS AOD spectra shown are for the 15 MODIS-Aqua grid cells for the 17.90 UT Aqua overpass on 8 August 2004, a case with AOD < 0.1 for all $\lambda > 400$ nm.

[69] To illustrate the effect of excluding cases with small AOD, Figure 17 (right) shows the MODIS-AATS Ångstrom scatterplot for all cells except those with AATS AOD(855) < 0.1. This exclusion markedly reduces RMS differences between MODIS and AATS Ångstrom exponents; however, the reduced range of AATS Ångstrom exponent values reduces most R^2 values as well.

[70] *Anderson et al.* [2005] also compared Ångstrom exponents from MODIS and airborne Sun photometer, using data from April 2001 near Japan and Korea involving varying mixtures of dust, sea salt, and pollution. As in the current study and *Redemann et al.* [2006b], *Anderson et al.*

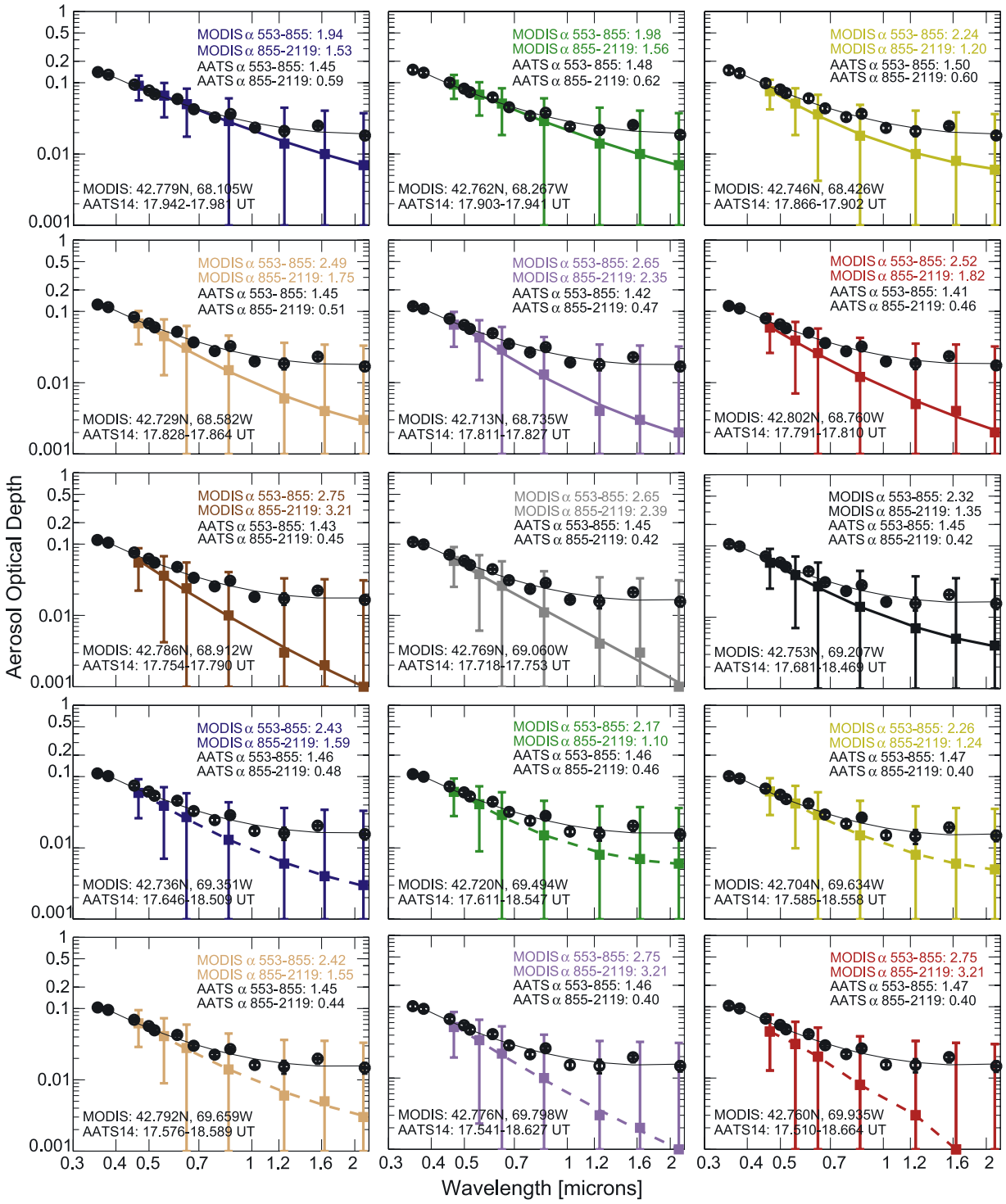

Figure 19. Comparison of AATS and MODIS AOD spectra and Ångstrom exponent values for 15 MODIS-Aqua grid cells of the 17.90 UT Aqua overpass on 8 August 2004.

[2005] found that Ångstrom exponents from MODIS were systematically larger than those from airborne Sun photometer. However, RMS differences found by *Anderson et al.* [2005] were only 0.14, considerably less than the RMS differences found in the current study (0.3 to 1.2) or by *Redemann et al.* [2006b] [0.2 to 0.7]. The fact that the *Anderson et al.* [2005] midvisible AODs (0.25 to 0.45 at 550 nm) included none of the small AODs of the *Redemann et al.* [2006b] and current studies may help explain the relatively small RMS differences found by *Anderson et al.* [2005] (The midvisible AOD range for *Redemann et al.* [2006b] was 0.13 to 0.3; for the MODIS-AATS comparisons of the current study it was 0.06 to 0.66.) However, relatively large AODs do not ensure small differences

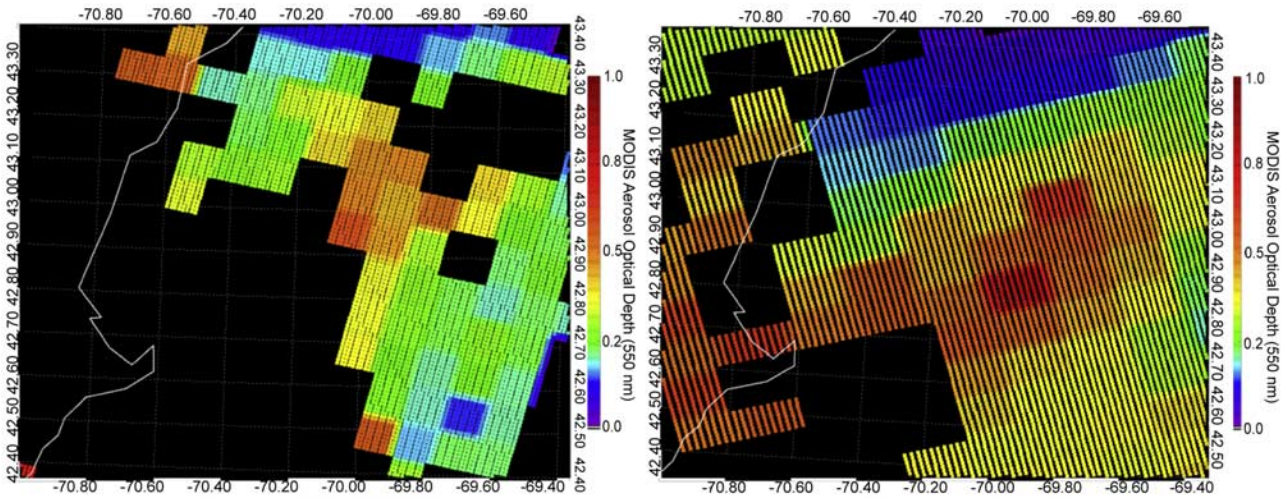

Figure 20. Fields of AOD retrieved from MODIS for 29 July 2004 with the glint mask reduced to 25°. (left) MODIS-Terra, 1535 UT. (right) MODIS-Aqua, 1715 UT.

between MODIS and suborbital results for Ångstrom exponent; other studies [e.g., *Levy et al.*, 2003; *Livingston et al.*, 2003] have found MODIS retrievals of Ångstrom exponent that differed significantly from suborbital results, possibly as a result of dust nonsphericity.

[71] As a final note on MODIS Ångstrom exponent comparisons, we report that we have repeated all the above analyses, using MODIS Ångstrom exponents from the single best solution in place of the average of a number of solutions that best matched the measured radiances, i.e., substituting MODIS [Ångstrom_Exponent_1_Ocean(1)] for [Ångstrom_Exponent_1_Ocean(2)], and [Ångstrom_Exponent_2_Ocean(1)] for [Ångstrom_Exponent_2_Ocean(2)]. The results (not shown for brevity) show the following: (1) Using the single-best-solution set of MODIS Ångstrom exponents produces scatterplots very similar to those in Figure 17, but with most RMS MODIS-AATS differences slightly smaller than those for the average of best solutions. (2) When AOD is small (e.g., on 8 August, Figure 19), large cell-to-cell jumps in α(855−2113 nm) occur for both the single-best-solution and average-of-best-solutions sets of MODIS Ångstrom exponent. From this we conclude that the single-best-solution set of MODIS Ångstrom exponents is slightly more accurate than the average-of-best-solutions set, and that use of the average-of-best-solutions set does not protect against large cell-to-cell jumps in α(855–2113 nm) when AOD becomes small enough.

3.5. Experiments With Extending MODIS Retrievals Into the Glint Mask

[72] Sun glint is the specular reflection of sunlight from the sea surface. All MODIS AOD results shown so far in this paper were obtained using the standard MODIS glint mask, which excludes from the AOD retrieval all pixels for which the glint angle ψ is <40° [cf. *Tanré et al.*, 1997, 1999]. For each pixel, ψ is defined as the angle between two light paths: the pixel-to-satellite path and the path of specular reflection of the solar beam assuming the pixel is a horizontal mirror.

[73] On 29 July 2004 the J31 underflew both Terra and Aqua, and its flight path was within the standard MODIS glint mask (i.e., ψ was <40°) for both MODIS-Terra and MODIS-Aqua. Hence the MODIS standard algorithm with the standard glint mask produced no AOD retrievals along the J31 flight path. To test whether MODIS AOD retrievals could succeed within the standard mask, we ran the AOD algorithm with the glint mask reduced below its normal cutoff of 40°. Figure 20 shows an example of the resulting AOD retrievals, in this case with both the MODIS-Terra and MODIS-Aqua glint masks reduced to 25°. Table 5 lists coordinates and other characteristics of the MODIS grid cells analyzed. Figure 21 shows the J31 flight path, with low-altitude segments flown near the Terra and Aqua overpass times (1534 and 1715 UT) indicated. (At 1534 UT the J31 was on the low-altitude path shown; at 1715 it was in a spiral, after which it flew the indicated low-altitude leg from 1727 to 1737 UT.)

[74] Figures 22 and 23 show the MODIS retrieval grid cells along the J31 low-level legs and compare the resulting MODIS AOD retrievals to the AATS AOD results. Glint angles within the MODIS-Terra cells shown range from 29.3° to 34.7°. For the MODIS-Aqua cells shown they range from 32.0° to 33.0°. Note that the MODIS AOD spectra systematically underestimate the AATS spectra, especially at the longer wavelengths. The sign of these AOD differences (MODIS AOD < AATS AOD) is consistent with wind speeds measured on board the NOAA R/V *Ronald H. Brown* (located as shown in Figure 21). Specifically, wind speed on the R/V *Ronald H. Brown* was 0.7 m s^{-1} at Terra overpass time and 3.4 m s^{-1} at Aqua overpass time. These speeds are both less than the 6 m s^{-1} assumed by the MODIS AOD retrieval algorithm in computing surface reflectance within the glint mask (using a rough-ocean model, as described by *Tanré et al.* [1999]). Hence the MODIS AOD retrievals assume more ocean reflectance than is actually present in these cases, and must retrieve less-than-actual AOD to match the observed radiances. Comparing Figures 22 and 23 shows that the MODIS-AATS AOD differences are less for MODIS-Aqua than for MODIS-Terra. This is consistent

Table 5. MODIS Cells for the 29 July 2004 Sun Glint Study

Date, 2004	Satellite	Overpass Time, UT		Grid Cell Center		AOD Retrieval Quality Flag[a]	Glint Angle, deg	AOD(553 nm)		a(553, 855 nm)		a(855, 2119 nm)	
		hhmm	Decimal h	Lon W	Lat N			MODIS	AATS	MODIS	AATS	MODIS	AATS
29 Jul	Terra	1534	15.57	70.374	43.295	1	34.77	0.084	0.322	2.750	1.430	3.210	1.790
29 Jul	Terra	1534	15.57	70.403	43.207	1	34.72	0.118	0.341	2.750	1.420	3.210	1.800
29 Jul	Terra	1534	15.57	70.280	43.190	1	33.91	0.105	0.404	2.750	1.380	3.210	1.840
29 Jul	Terra	1534	15.57	70.157	43.173	1	33.11	0.107	0.456	2.750	1.360	3.210	1.880
29 Jul	Terra	1534	15.57	70.035	43.156	1	32.33	0.128	0.479	2.750	1.360	3.210	1.960
29 Jul	Terra	1534	15.57	69.913	43.138	1	31.55	0.166	0.589	2.750	1.320	3.210	1.990
29 Jul	Terra	1534	15.57	69.791	43.121	1	30.80	0.213	0.658	2.750	1.300	3.210	2.020
29 Jul	Terra	1534	15.57	69.670	43.103	1	30.03	0.289	0.861	2.750	1.160	3.210	1.980
29 Jul	Terra	1534	15.57	69.549	43.086	1	29.31	0.310	0.935	2.750	1.070	3.210	1.820
29 Jul	Terra	1534	15.57	70.308	43.102	1	33.86	0.188	0.459	2.750	1.370	3.210	1.900
29 Jul	Terra	1534	15.57	70.186	43.085	1	33.06	0.236	0.544	2.750	1.340	3.210	1.970
29 Jul	Terra	1534	15.57	70.214	42.996	1	33.00	0.345	0.613	2.750	1.330	3.210	2.020
29 Jul	Terra	1534	15.57	70.093	42.979	1	32.22	0.399	0.695	2.750	1.280	3.210	1.980
29 Jul	Terra	1534	15.57	70.000	42.874	1	31.38	0.492	0.902	2.750	1.170	3.210	1.930
29 Jul	Terra	1534	15.57	69.638	42.821	1	29.13	0.291	0.879	2.750	1.180	3.210	1.970
29 Jul	Terra	1534	15.57	69.908	42.768	1	30.56	0.511	1.022	2.750	1.170	3.210	1.980
29 Jul	Terra	1534	15.57	69.788	42.751	1	29.79	0.361	0.761	2.750	1.300	3.210	2.060
29 Jul	Terra	1534	15.57	69.667	42.733	1	29.06	0.243	0.809	2.750	1.240	3.210	2.010
29 Jul	Aqua	1710	17.17	69.994	42.681	1	32.03	0.567	0.744	2.750	1.240	3.210	1.750
29 Jul	Aqua	1710	17.17	70.034	42.768	1	32.07	0.511	0.583	2.750	1.270	3.210	1.690
29 Jul	Aqua	1710	17.17	70.072	42.854	1	32.11	0.432	0.575	2.750	1.240	3.210	1.670
29 Jul	Aqua	1710	17.17	70.266	42.814	1	32.94	0.551	0.678	1.870	1.090	2.950	1.610
29 Jul	Aqua	1710	17.17	70.306	42.901	1	32.99	0.294	0.489	2.750	1.270	3.210	1.620
29 Jul	Aqua	1710	17.17	70.345	42.987	1	33.02	0.225	0.391	2.750	1.320	3.210	1.510

[a]0, no confidence; 1, marginal; 2, good; 3, very good.

with the ship-measured increase in wind speed, from 0.7 m s^{-1} at Terra overpass time to 3.4 m s^{-1} at Aqua overpass time. In other words, wind speed at Aqua overpass time is closer to the assumed 6 m s^{-1}, leading to less underestimation in retrieved AOD. As noted in section 2.3.1, differences between MODIS-Terra and MODIS-Aqua level 2 products have been noted before when dust was present; however, since dust was not present in this case, we feel the Terra-Aqua wind speed difference is likely to be the main reason for the Terra-Aqua differences in MODIS-AATS AOD differences.

[75] The fact that significant underestimation in MODIS-retrieved AOD is obtained even for the cell with the largest glint angle, 34.7°, in Figure 22, indicates that the standard MODIS glint mask cutoff angle, 40°, should not be reduced by as much as 5° below its current value. This is consistent with Figure 15 of *Tanré et al.* [1999], which shows glint-induced errors in AOD (from the MODIS airborne simulator) increasing rapidly for glint angle decreasing from 38° to 34°.

4. Summary and Conclusions

[76] Sun photometer measurements on low-altitude J31 transects in summer 2004 provided AOD spectra for comparison to satellite retrievals in 29 MISR grid cells (on 20, 22, and 29 July and 7 August), in 17 MODIS-Terra standard AOD retrieval grid cells (on 17 and 22 July and 2 August), and 44 MODIS-Aqua standard AOD retrieval grid cells (on 12, 16, 21, and 23 July and 8 August), plus 14 MODIS-Terra and 6 MODIS-Aqua cells that were excluded by the standard MODIS glint mask on 29 July. Each grid cell had J31 altitude 60 to 100 m and AATS measurements within 30 min of satellite overpass time, with several exceptions: 7 grid cells where J31 altitude was as high as 110 to 250 m and 2 cells with J31 measurement time extending to 31 and 33 min after satellite overpass. In each exceptional cell the AATS-satellite AOD comparisons were essentially the same as in neighboring cells where J31 altitude was <100 m and AATS measurement time was within 30 min of satellite overpass.

[77] Ship measurements of humidified light scattering and absorption during six J31 flybys were used to estimate AOD below the J31. In all six cases the estimated midvisible

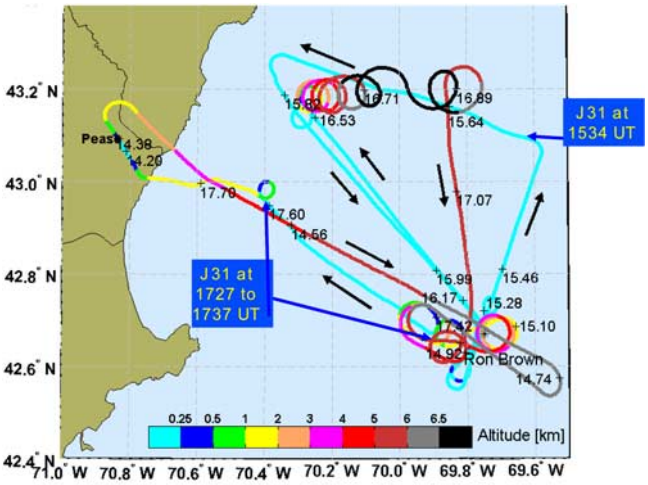

Figure 21. J31 flight path on 29 July 2004, underflying both Terra (1534 UT) and Aqua at or near minimum altitude (60 to 100 m).

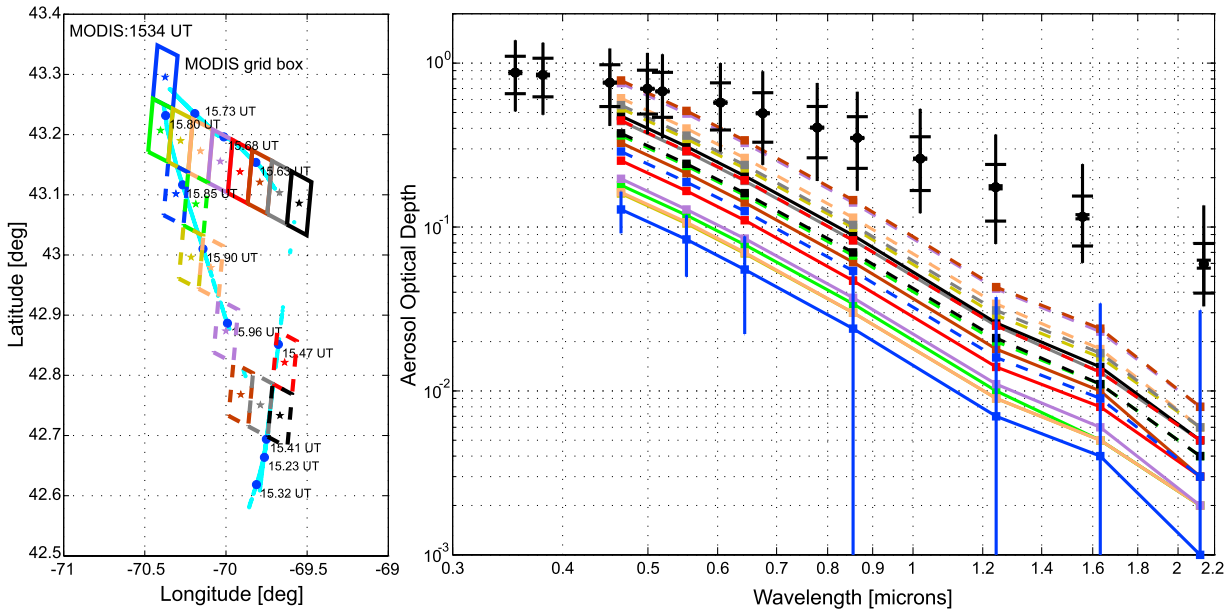

Figure 22. Comparison of AATS and MODIS-Terra AOD spectra for the 29 July 2004 1534 UT Terra overpass. Left frame shows 16 MODIS grid cells that yielded AOD retrievals along the J31 low-altitude path. Resulting AOD spectra are color coded by grid cell color. The AATS spectrum (open black circles) is a mean from the whole low-altitude flight path shown, along with the typical AATS measurement uncertainty (narrow ticks), standard deviation of results along the flight path (wide ticks), and range along the flight path (vertical bars).

AOD below the J31 was <0.014 (typically <0.01) when the J31 was at the typical altitude of 60 to 100 m ASL used in its low-altitude transects. These values are comparable to the typical Sun photometer calibration uncertainty of ~0.01. The ratios of AOD(500 nm) below the J31 to AOD(500 nm) above the J31 ranged from 1.0% to 13.7%, with mean value 6.2% and standard deviation 4.8%. Including four wavelengths, 450–700 nm, the mean ratio of AOD below to above the J31 ranged from 5.9% to 6.3% with standard deviation 4.5% to 5.4%.

[78] This paper presents results for MISR-AATS AOD comparisons on 29 July 2004 in 8 grid cells (each 17.6 km ×

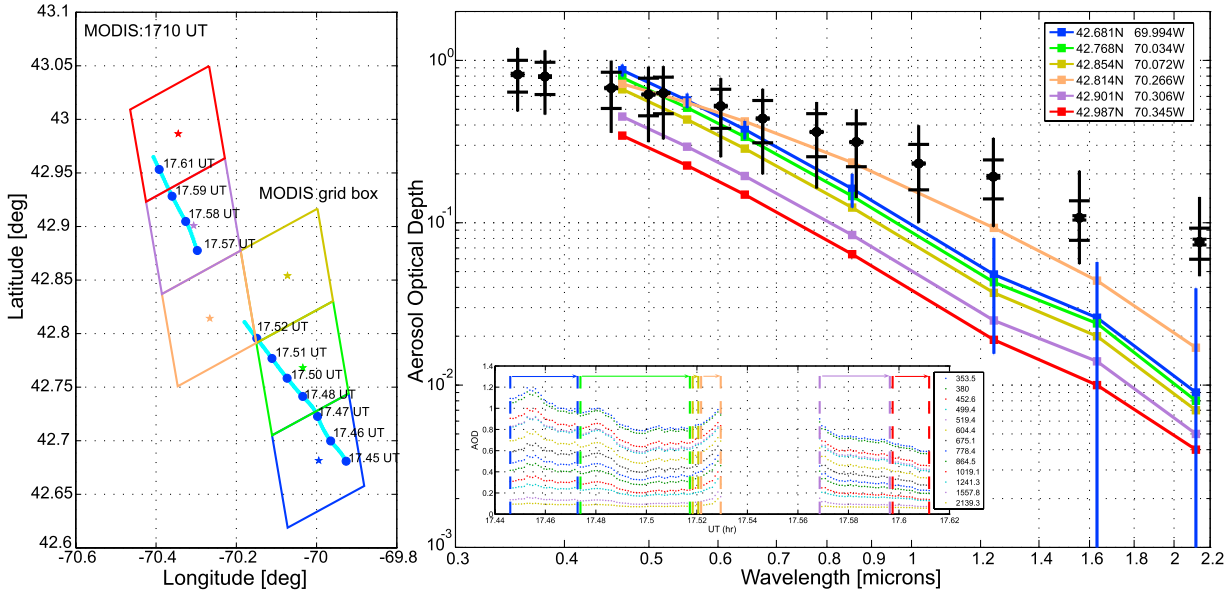

Figure 23. As in Figure 22 but for AATS and MODIS-Aqua AOD spectra for the 29 July 2004 1710 UT Aqua overpass, corresponding J31 low-altitude path, and 6 corresponding grid cells.

17.6 km). On this day AATS measurements in the MISR footprint showed a strong AOD gradient, with AOD(500 nm) changing by as much as 0.13 per 10 km in the horizontal. MISR-AATS AOD comparisons show that MISR version 15 and 16 retrievals also documented a gradient: MISR and AATS AODs were highly correlated, with $R^2 = 0.87$ to 0.92. However, the MISR gradient was somewhat weaker than the AATS gradient. The large AOD (midvisible values up to ~0.8) and differing gradients in this case produced root-mean-square (RMS) MISR-AATS AOD differences of 0.03 to 0.21 (9 to 31%). MISR V15 Ångstrom exponent α was closer to AATS than was MISR V16. These and other analyses are being used to improve the MISR retrievals, including their information on such aerosol microphysical properties as size and absorption.

[79] MODIS-AATS AOD comparisons on 8 overpasses using the standard MODIS glint mask in 61 grid cells (each nominally 10 km × 10 km) had $R^2 \sim 0.97$, with RMS AOD difference ~0.03 (~20%). About 87% of the MODIS AOD retrievals (89% for Aqua, 81% for Terra) differed from AATS values by less than the predicted MODIS over-ocean uncertainty, $\Delta\tau = \pm 0.03 \pm 0.05\tau$. In contrast to the small MODIS-AATS differences in AOD, MODIS-AATS differences in Ångstrom exponent α were large: RMS differences for α(553, 855 nm) were 0.28 for MODIS-Terra and 0.64 for MODIS-Aqua; RMS differences for α(855, 2119 nm) were larger still: 0.61 for MODIS-Terra and 1.14 for MODIS-Aqua. None of the four correlation coefficients for Ångstrom exponent had $R^2 > 0.7$. The largest MODIS-AATS Ångstrom exponent differences were associated with small AOD values, for which MODIS AOD relative uncertainty is large. Excluding cases with AOD(855 nm) < 0.1 reduced MODIS-AATS α differences markedly; resulting RMS differences for α(553, 855 nm) were 0.18 for MODIS-Terra and 0.13 for MODIS-Aqua; RMS differences for α(855, 2119 nm) were 0.46 for MODIS-Terra and 0.41 for MODIS-Aqua.

[80] In one grid cell on 21 July 2004, smoke over cloud appeared to impair the MODIS-Aqua cloud mask, resulting in retrieved AODs that significantly exceeded the AATS values. Evidence for cloud effects on MODIS AOD in this case includes not only AOD values but also differences in Ångstrom exponents and an increased cloud frequency in both the AATS data record and in the MODIS retrieval itself.

[81] Experiments with extending MODIS retrievals into 14 MODIS-Terra and 6 MODIS-Aqua cells within the standard MODIS glint mask on 29 July yielded MODIS AODs consistently less than AATS AODs, especially at long wavelength, indicating that the current MODIS glint mask limits should not be reduced to the extent tried here. The sign of these AOD differences (MODIS AOD < AATS AOD) is consistent with wind speeds measured on board the NOAA R/V *Ronald H. Brown*. The fact that the MODIS-AATS AOD differences within the glint mask were less for MODIS-Aqua than for MODIS-Terra is consistent with the ship-measured increase in wind speed, from 0.7 m s^{-1} at Terra overpass time to 3.4 m s^{-1} at Aqua overpass time.

[82] **Acknowledgments.** This research is a contribution to the International Consortium for Atmospheric Research on Transport and Transformation (ICARTT), which includes Phase A of the Intercontinental Chemical Transport Experiment (INTEX-A) of NASA and the Intercontinental Transport and Chemical Transformation (ITCT) experiment of NOAA. The AATS-14 measurements were supported by NOAA's Atmospheric Composition and Climate Program and by NASA's Programs in Radiation Science, Suborbital Science, and Tropospheric Chemistry. The analyses were supported by NASA's Earth Observing System Inter-Disciplinary Science (EOS-IDS) Program. The work of R. Kahn is supported in part by NASA's Climate and Radiation Research and Analysis Program, under H. Maring, and in part by the EOS-MISR instrument project; it is performed at the Jet Propulsion Laboratory, California Institute of Technology, under contract with NASA.

References

Abdou, W. A., D. J. Diner, J. V. Martonchik, C. J. Bruegge, R. A. Kahn, B. J. Gaitley, K. A. Crean, L. A. Remer, and B. Holben (2005), Comparison of coincident Multiangle Imaging Spectroradiometer and Moderate Resolution Imaging Spectroradiometer aerosol optical depths over land and ocean scenes containing Aerosol Robotic Network sites, *J. Geophys. Res.*, *110*, D10S07, doi:10.1029/2004JD004693.

Anderson, T. L., and J. A. Ogren (1998), Determining aerosol radiative properties using the TSI 3563 integrating nephelometer, *Aerosol Sci. Technol.*, *29*, 57–69.

Anderson, T. L., Y. Wu, D. A. Chu, B. Schmid, J. Redemann, and O. Dubovik (2005), Testing the MODIS satellite retrieval of aerosol fine-mode fraction, *J. Geophys. Res.*, *110*, D18204, doi:10.1029/2005JD005978.

Bevington, P. R. (1969), *Data Reduction and Error Analysis for the Physical Sciences*, 336 pp., McGraw-Hill, New York.

Carrico, C., P. Kus, M. Rood, P. Quinn, and T. Bates (2003), Mixtures of pollution, dust, seasalt, and volcanic aerosol during ACE-Asia: Aerosol radiative properties as a function of relative humidity, *J. Geophys. Res.*, *108*(D23), 8650, doi:10.1029/2003JD003405.

Chu, D. A., Y. J. Kaufman, C. Ichoku, L. A. Remer, D. Tanré, and B. N. Holben (2002), Validation of MODIS aerosol optical depth retrieval over land, *Geophys. Res. Lett.*, *29*(12), 8007, doi:10.1029/2001GL013205.

Chu, D. A., et al. (2005), Evaluation of aerosol properties over ocean from Moderate Resolution Imaging Spectroradiometer (MODIS) during ACE-Asia, *J. Geophys. Res.*, *110*, D07308, doi:10.1029/2004JD005208.

Di Girolamo, L., and M. J. Wilson (2003), A first look at band-differenced angular signatures for cloud detection from MISR, *IEEE Trans. Geosci. Remote Sens.*, *41*, 1730–1734.

Diner, D. J., et al. (1998), Multiangle Imaging Spectroradiometer (MISR) description and experiment overview, *IEEE Trans. Geosci. Remote Sens.*, *36*, 1072–1087.

Fehsenfeld, F. C., et al. (2006), International Consortium for Atmospheric Research on Transport and Transformation (ICARTT): North America to Europe—Overview of the 2004 summer field study, *J. Geophys. Res.*, *111*, D23S01, doi:10.1029/2006JD007829.

Gao, B., Y. J. Kaufman, D. Tanre, and R. Li (2002), Distinguishing tropospheric aerosols from thin cirrus clouds for improved aerosol retrievals using the ratio of 1.38-μm and 1.24-μm channels, *Geophys. Res. Lett.*, *29*(18), 1890, doi:10.1029/2002GL015475.

Gassó, S., and N. O'Neill (2006), Comparisons of remote sensing retrievals and in situ measurements of aerosol fine mode fraction during ACE-Asia, *Geophys. Res. Lett.*, *33*, L05807, doi:10.1029/2005GL024926.

Gassó, S., N. T. O'Neill, and J. Redemann (2004), Passive remote sensing of aerosol fine mode fraction: A comparison with in-situ measurements during the ACE-Asia field campaign, *Eos Trans. AGU*, *85*(47), Fall Meet. Suppl., Abstract A33D-0095.

Huebert, B. J., T. Bates, P. B. Russell, G. Shi, Y. J. Kim, K. Kawamura, G. Carmichael, and T. Nakajima (2003), An overview of ACE-Asia: Strategies for quantifying the relationships between Asian aerosols and their climatic impacts, *J. Geophys. Res.*, *108*(D23), 8633, doi:10.1029/2003JD003550.

Ichoku, C., D. A. Chu, S. Mattoo, Y. J. Kaufman, L. A. Remer, D. Tanré, I. Slutsker, and B. N. Holben (2002), A spatio-temporal approach for global validation and analysis of MODIS aerosol products, *Geophys. Res. Lett.*, *29*(12), 8006, doi:10.1029/2001GL013206.

Ichoku, C., L. A. Remer, and T. F. Eck (2005), Quantitative evaluation and intercomparison of morning and afternoon MODIS aerosol measurements from Terra and Aqua, *J. Geophys. Res.*, *110*, D10S03, doi:10.1029/2004JD004987.

Kahn, R., P. Banerjee, and D. McDonald (2001a), Sensitivity of multiangle imaging to natural mixtures of aerosols over ocean, *J. Geophys. Res.*, *106*, 18,219–18,238.

Kahn, R., P. Banerjee, D. McDonald, and J. Martonchik (2001b), Aerosol properties derived from aircraft multi-angle imaging over Monterey Bay, *J. Geophys. Res.*, *106*, 11,977–11,995.

Kahn, R., et al. (2004), Environmental snapshots from ACE-Asia, *J. Geophys. Res.*, *109*, D19S14, doi:10.1029/2003JD004339.

Kahn, R. A., B. J. Gaitley, J. V. Martonchik, D. J. Diner, K. A. Crean, and B. Holben (2005), Multiangle Imaging Spectroradiometer (MISR) global aerosol optical depth validation based on 2 years of coincident Aerosol Robotic Network (AERONET) observations, *J. Geophys. Res.*, *110*, D10S04, doi:10.1029/2004JD004706.

Kalashnikova, O. V., and R. Kahn (2006), Ability of multiangle remote sensing observations to identify and distinguish mineral dust types: 2. Sensitivity over dark water, *J. Geophys. Res.*, *111*, D11207, doi:10.1029/2005JD006756.

Kalashnikova, O. V., R. Kahn, I. N. Sokolik, and W.-H. Li (2005), Ability of multiangle remote sensing observations to identify and distinguish mineral dust types: Optical models and retrievals of optically thick plumes, *J. Geophys. Res.*, *110*, D18S14, doi:10.1029/2004JD004550.

Kaufman, Y. J., D. Tanré, L. A. Remer, E. Vermote, A. Chu, and B. N. Holben (1997), Operational remote sensing of tropospheric aerosol over land from EOS moderate resolution imaging spectroradiometer, *J. Geophys. Res.*, *102*, 17,051–17,067.

Kaufman, Y. J., D. Tanré, and O. Boucher (2002), A satellite view of aerosols in the climate system, *Nature*, *419*, 215–223.

Levy, R. C., L. A. Remer, D. Tanré, Y. J. Kaufman, C. Ichoku, B. N. Holben, J. M. Livingston, P. B. Russell, and H. Maring (2003), Evaluation of the Moderate-Resolution Imaging Spectroradiometer (MODIS) retrievals of dust aerosol over the ocean during PRIDE, *J. Geophys. Res.*, *108*(D19), 8594, doi:10.1029/2002JD002460.

Levy, R. C., L. A. Remer, J. V. Martins, Y. J. Kaufman, A. Plana-Fattori, J. Redemann, and B. Wenny (2005), Evaluation of the MODIS aerosol retrievals over ocean and land during CLAMS, *J. Atmos. Sci.*, *62*, 974–992.

Livingston, J. M., et al. (2003), Airborne sunphotometer measurements of aerosol optical depth and columnar water vapor during the Puerto Rico Dust Experiment, and comparison with land, aircraft, and satellite measurements, *J. Geophys. Res.*, *108*(D19), 8588, doi:10.1029/2002JD002520.

Livingston, J. M., et al. (2007), Comparison of water vapor measurements by airborne Sun photometer and near-coincident in situ and satellite sensors during INTEX-ITCT 2004, *J. Geophys. Res.*, doi:10.1029/2006JD007733, in press.

Martins, J. V., D. Tanré, L. Remer, Y. Kaufman, S. Mattoo, and R. Levy (2002), MODIS Cloud screening for remote sensing of aerosols over oceans using spatial variability, *Geophys. Res. Lett.*, *29*(12), 8009, doi:10.1029/2001GL013252.

Martonchik, J. V., D. J. Diner, R. Kahn, M. M. Verstraete, B. Pinty, H. R. Gordon, and T. P. Ackerman (1998), Techniques for the retrieval of aerosol properties over land and ocean using multiangle imaging, *IEEE Trans. Geosci. Remote Sens.*, *36*, 1212–1227.

Martonchik, J. V., D. J. Diner, R. Kahn, B. Gaitley, and B. N. Holben (2004), Comparison of MISR and AERONET aerosol optical depths over desert sites, *Geophys. Res. Lett.*, *31*, L16102, doi:10.1029/2004GL019807.

McArthur, L. J. B., D. H. Halliwell, O. J. Niebergall, N. T. O'Neill, J. R. Slusser, and C. Wehrli (2003), Field comparison of network Sun photometers, *J. Geophys. Res.*, *108*(D19), 4596, doi:10.1029/2002JD002964.

Michalsky, J. J., J. C. Liljegren, and L. C. Harrison (1995), A comparison of sun photometer derivations of total column water vapor and ozone to standard measures of same at the Southern Great Plains Atmospheric Radiation Measurement site, *J. Geophys. Res.*, *100*, 25,995–26,003.

Moroney, C., R. Davies, and J.-P. Muller (2002), Operational retrieval of cloud-top heights using MISR data, *IEEE Trans. Geosci. Remote Sens.*, *40*, 1532–1540, doi:10.1109/TGRS.2002.801150.

Nikolaeva, O. V., L. P. Bass, T. A. Germogenova, A. A. Kokhanovsky, V. S. Kuznetsov, and B. Mayer (2005), The influence of neighbouring clouds on the clear sky reflectance studied with the 3-D transport code RADUGA, *J. Quant. Spectrosc. Radiat. Transfer*, *94*, 405–424.

Ramanathan, V., P. J. Crutzen, J. T. Kiehl, and D. Rosenfeld (2001), Aerosol, climate and the hydrological cycle, *Science*, *294*, 2119–2124.

Reagan, J., K. Thome, B. Herman, R. Stone, J. Deluisi, and J. Snider (1995), A comparison of columnar water-vapor retrievals obtained with near-IR solar radiometer and microwave radiometer measurements, *J. Appl. Meteorol.*, *34*, 1384–1391.

Redemann, J. (2004), A comparison of level-3 aerosol products from various sensors in the Pacific basin, paper presented at MISR Science Team Meeting, Pasadena, Calif., Dec.

Redemann, J., P. B. Russell, and P. Hamill (2001), Dependence of aerosol light absorption and single scattering albedo on ambient relative humidity for sulfate aerosols with black carbon cores, *J. Geophys. Res.*, *106*, 27,485–27,495.

Redemann, J., S. Masonis, B. Schmid, T. Anderson, P. Russell, J. Livingston, O. Dubovik, and A. Clarke (2003), Clear-column closure studies of aerosols and water vapor aboard the NCAR C-130 in ACE-Asia, 2001, *J. Geophys. Res.*, *108*(D23), 8655, doi:10.1029/2003JD003442.

Redemann, J., P. B. Russell, and R. W. Bergstrom (2004), Aerosol-induced radiative flux changes in the Pacific Basin troposphere, *Eos Trans. AGU*, *85*(46), Fall Meet. Suppl., Abstract A11C-0080.

Redemann, J., B. Schmid, J. A. Eilers, R. A. Kahn, R. C. Levy, P. B. Russell, J. M. Livingston, P. V. Hobbs, W. L. Smith Jr., and B. N. Holben (2005), Suborbital measurements of spectral aerosol optical depth and its variability at sub-satellite grid scales in support of CLAMS, 2001, *J. Atmos. Sci.*, *62*(4), 993–1007.

Redemann, J., P. Pilewskie, P. B. Russell, J. M. Livingston, S. Howard, B. Schmid, J. Pommier, W. Gore, J. Eilers, and M. Wendisch (2006a), Airborne measurements of spectral direct aerosol radiative forcing in the Intercontinental Chemical Transport Experiment/Intercontinental Transport and Chemical Transformation of anthropogenic pollution, 2004, *J. Geophys. Res.*, *111*, D08S11, doi:10.1029/2005JD006017.

Redemann, J., Q. Zhang, B. Schmid, P. B. Russell, J. M. Livingston, H. Jonsson, and L. A. Remer (2006b), Assessment of MODIS-derived visible and near-IR aerosol optical properties and their spatial variability in the presence of mineral dust, *Geophys. Res. Lett.*, *33*, L18814, doi:10.1029/2006GL026626.

Remer, L. A., and Y. J. Kaufman (2006), Aerosol direct radiative effect at the top of the atmosphere over cloud free ocean derived from four years of MODIS data, *Atmos. Phys. Chem.*, *6*, 237–253.

Remer, L. A., et al. (2002), Validation of MODIS aerosol retrieval over ocean, *Geophys. Res. Lett.*, *29*(12), 8008, doi:10.1029/2001GL013204.

Remer, L. A., et al. (2005), The MODIS aerosol algorithm, products and validation, *J. Atmos. Sci.*, *62*, 947–973.

Rood, M. J., W. Wang, C. M. Carrico, D. S. Covert, P. K. Quinn, and T. S. Bates (2006), Aerosol optical properties along the northeast coast of North America during NEAQS-ITCT 2004, and the influence of aerosol composition, *J. Geophys. Res.*, doi:10.1029/2006JD007579, in press.

Russell, P. B., et al. (1993a), Pinatubo and pre-Pinatubo optical-depth spectra: Mauna Loa measurements, comparisons, inferred particle size distributions, radiative effects, and relationship to lidar data, *J. Geophys. Res.*, *98*, 22,969–22,985.

Russell, P. B., et al. (1993b), Post-Pinatubo optical depth spectra vs. latitude and vortex structure: Airborne tracking sunphotometer measurements in AASE II, *Geophys. Res. Lett.*, *20*, 2571–2574.

Russell, P., et al. (2005), Aerosol optical depth measurements by airborne Sun photometer in SOLVE II: Comparisons to SAGE III, POAM III and airborne spectrometer measurements, *Atmos. Chem. Phys.*, *5*, 1311–1339, SRef-ID:1680-7324/acp/2005-5-1311.

Schmid, B., and C. Wehrli (1995), Comparison of sun photometer calibration by Langley technique and standard lamp, *Appl. Opt.*, *34*, 4500–4512.

Schmid, B., K. J. Thome, P. Demoulin, R. Peter, C. Matzler, and J. Sekler (1996), Comparison of modeled and empirical approaches for retrieving columnar water vapor from solar transmittance measurements in the 0.94-μm region, *J. Geophys. Res.*, *101*, 9345–9358.

Schmid, B., P. R. Spyak, S. F. Biggar, C. Wehrli, J. Sekler, T. Ingold, C. Mätzler, and N. Kämpfer (1998), Evaluation of the applicability of solar and lamp radiometric calibrations of a precision Sun photometer operating between 300 and 1025 nm, *Appl. Opt.*, *37*, 3923–3941.

Schmid, B., et al. (2000), Clear sky closure studies of lower tropospheric aerosol and water vapor during ACE 2 using airborne sunphotometer, airborne in-situ, space-borne, and ground-based measurements, *Tellus, Ser. B*, *52*, 568–593.

Schmid, B., et al. (2001), Comparison of columnar water-vapor measurements from solar transmittance methods, *Appl. Opt.*, *40*, 1886–1896.

Schmid, B., et al. (2003a), Coordinated airborne, spaceborne, and ground-based measurements of massive, thick aerosol layers during the dry season in Southern Africa, *J. Geophys. Res.*, *108*(D13), 8496, doi:10.1029/2002JD002297.

Schmid, B., et al. (2003b), Column closure studies of lower tropospheric aerosol and water vapor during ACE-Asia using airborne sunphotometer, airborne in situ and ship-based lidar measurements, *J. Geophys. Res.*, *108*(D23), 8656, doi:10.1029/2002JD003361.

Schmid, B., et al. (2006), How well do state-of-the-art techniques measuring the vertical profile of tropospheric aerosol extinction compare?, *J. Geophys. Res.*, *111*, D05S07, doi:10.1029/2005JD005837.

Singh, H. B., W. H. Brune, J. H. Crawford, D. J. Jacob, and P. B. Russell (2006), Overview of the summer 2004 Intercontinental Chemical Transport Experiment–North America (INTEX-A), *J. Geophys. Res.*, *111*, D24S01, doi:10.1029/2006JD007905.

Smith, W. L., Jr., T. P. Charlock, R. Kahn, J. V. Martins, L. A. Remer, P. V. Hobbs, J. Redemann, and C. K. Rutledge (2005), EOS-TERRA aerosol and radiative flux validation: An overview of the Chesapeake Lighthouse and Aircraft Measurements for Satellites (CLAMS) experiment, *J. Atmos. Sci.*, *62*(4), 903–918, doi:10.1175/JAS3398.1.

Tanré, D., Y. J. Kaufman, M. Herman, and S. Matto (1997), Remote sensing of aerosol properties over oceans using the MODIS/EOS spectral radiance, *J. Geophys. Res.*, *102*, 16,971–16,988.

Tanré, D., L. A. Remer, Y. J. Kaufman, S. Mattoo, P. V. Hobbs, J. M. Livingston, P. B. Russell, and A. Smirnov (1999), Retrieval of aerosol optical thickness and size distribution over ocean from the MODIS airborne simulator during TARFOX, *J. Geophys. Res.*, *104*(D2), 2261–2278.

Wen, G. Y., A. Marshak, and R. F. Cahalan (2006), Impact of 3-D clouds on clear-sky reflectance and aerosol retrieval in a biomass burning region of Brazil, *IEEE Geosci. Remote Sens. Lett.*, *3*(1), 169–172.

Zhao, G., and L. Di Girolamo (2004), A cloud fraction versus view angle technique for automatic in-scene evaluation of the MISR cloud mask, *J. Appl. Meteorol.*, *43*(6), 860–869.

D. A. Chu and L. Remer, Laboratory for Atmospheres, NASA Goddard Space Flight Center, Code 912, Greenbelt, MD 20771, USA. (achu@climate.gsfc.nasa.gov)

J. Eilers and P. B. Russell, NASA Ames Research Center, MS 245-5, Moffett Field, CA 94035-1000, USA. (james.a.eilers@nasa.gov; philip.b.russell@nasa.gov)

R. A. Kahn, Jet Propulsion Lab, MS 169-237, 4800 Oak Grove Drive, Pasadena, CA 91109-8099, USA. (ralph.kahn@jpl.nasa.gov)

J. M. Livingston, SRI International, 333 Ravenswood Avenue, Menlo Park, CA 94025, USA. (jlivingston@mail.arc.nasa.gov)

P. K. Quinn, Pacific Marine Environmental Laboratory, NOAA, 7600 Sandpoint Way NE, Seattle, WA 98115, USA. (patricia.k.quinn@noaa.gov)

S. A. Ramirez, J. Redemann, and B. Schmid, Bay Area Environmental Research Institute, 560 3rd Street West, Sonoma, CA 95476, USA. (s.a.ramirez@mail.arc.nasa.gov; jredemann@mail.arc.nasa.gov; bschmid@mail.arc.nasa.gov)

M. J. Rood and W. Wang, Environmental Engineering and Science, Department of Civil and Environmental Engineering, University of Illinois at Urbana-Champaign, 3213 NCEL/MC-250, 205 N. Mathews Avenue, Urbana, IL 61801-2352, USA. (mrood@uiuc.edu; weiwang@uiuc.edu)